CrossMark

J. Fluid Mech. (2016), *vol.* 794, *pp.* 565–594. © Cambridge University Press 2016
doi:10.1017/jfm.2016.157

Lock-in in vortex-induced vibration

Navrose[1] **and Sanjay Mittal**[1,†]

[1]Department of Aerospace Engineering, Indian Institute of Technology Kanpur, Kanpur, UP 208016, India

(Received 31 May 2015; revised 29 December 2015; accepted 21 February 2016; first published online 5 April 2016)

The phenomenon of lock-in in vortex-induced vibration of a circular cylinder is investigated in the laminar flow regime ($20 \leqslant Re \leqslant 100$). Direct time integration (DTI) and linear stability analysis (LSA) of the governing equations are carried out via a stabilized finite element method. Using the metrics that have been proposed in earlier studies, the lock-in regime is identified from the results of DTI. The LSA yields the eigenmodes of the coupled fluid–structure system, the associated frequencies (F_{LSA}) and the stability of the steady state. A linearly unstable system, in the absence of nonlinear effects, achieves large oscillation amplitude at sufficiently large times. However, the nonlinear terms saturate the response of the system to a limit cycle. For subcritical Re, the occurrence of lock-in coincides with the linear instability of the fluid–structure system. The critical Re is the Reynolds number beyond which vortex shedding ensues for a stationary cylinder. For supercritical Re, even though the aeroelastic system is unstable for all reduced velocities (U^*) lock-in occurs only for a finite range of U^*. We present a method to estimate the time beyond which the nonlinear effects are expected to be significant. It is observed that much of the growth in the amplitude of cylinder oscillation takes place in the linear regime. The response of the cylinder at the end of the linear regime is found to depend on the energy ratio, E_r, of the unstable eigenmode. E_r is defined as the fraction of the total energy of the eigenmode that is associated with the kinetic and potential energy of the structure. DTI initiated from eigenmodes that are linearly unstable and whose energy ratio is above a certain threshold value lead to lock-in. Interestingly, during lock-in, the oscillation frequency of the fluid–structure system drifts from F_{LSA} towards a value that is closer to the natural frequency of the oscillator in vacuum (F_N). In the event of more than one eigenmode being linearly unstable, we investigate which one is responsible for lock-in. The concept of phase angle between the cylinder displacement and lift is extended for an eigenmode. The phase angle controls the direction of energy transfer between the fluid and the structure. For zero structural damping, if the phase angle of all unstable eigenmodes is less than 90°, the phase angle obtained via DTI evolves to a value that is close to 0°. If, on the other hand, the phase angle of any unstable eigenmode is more than 90°, it settles to 180°, approximately in the limit cycle. A new approach towards classification of modes is presented. The eigenvalues are tracked over a wide range of U^* while keeping Re and mass ratio (m^*) fixed. In general, for large values of m^*, the eigenmodes corresponding to the two leading eigenvalues exhibit a decoupled behaviour with respect to U^*. They are classified as

† Email address for correspondence: smittal@iitk.ac.in

https://doi.org/10.1017/jfm.2016.157 Published online by Cambridge University Press

the fluid and elastic modes. However, for relatively low m^* such a classification is not possible. The two leading modes are coupled and are referred to as fluid–elastic modes. The regime of such occurrence is shown on the Re–m^* parameter space.

Key words: flow–structure interaction, parametric instability, vortex-shedding

1. Introduction

Lock-in/synchronization/wake-capture is an important phenomenon associated with vortex-induced vibrations (VIV) of bluff bodies. It is characterized by a high amplitude of structural vibrations. These vibrations can cause fatigue and may lead to catastrophic failure of structures. Lock-in, therefore, has been a subject of numerous computational and experimental studies in the past. For a detailed review on the various works that have been carried out related to synchronization in VIV, the interested reader is referred to articles by Bearman (1984, 2011), Sarpkaya (2004), Williamson & Govardhan (2004) and Wu, Ge & Hong (2012). Most of the earlier studies on VIV have focused on characterizing the lock-in regime, and its dependence on various parameters. In this paper, we explore the mechanism that leads to the phenomenon of lock-in.

First, we present a very brief review of the studies that mainly focus on characterizing the fluid–structure system within the lock-in regime. The behaviour of the fluid–structure system depends very significantly on the Reynolds number (Re) and mass of the cylinder. As a result, depending on the parameter range over which the various studies have been carried out, several definitions of lock-in have been proposed/used in the literature. The pioneering work by Bishop & Hassan (1964) and Feng (1968) shows that during lock-in, the frequency of cylinder oscillation is close to the natural frequency of the oscillator. In these two studies the fluid medium surrounding the cylinder was air. Hence, the mass ratio, m^*, defined as the ratio of the mass of the moving structure to the mass of the displaced fluid is high ($m^* \sim O(100)$). Khalak & Williamson (1997, 1999) carried out experiments with relatively low mass ratios ($m^* \sim O(10)$) by conducting experiments in water. The range of Reynolds number for these experiments varied between $5000 \leqslant Re \leqslant 16\,000$. They observed large amplitude oscillations of the cylinder with a frequency that is significantly higher than the natural frequency of the oscillator in water. In such cases, they found that the pattern of vortex shedding is different from that of the flow past a stationary cylinder and repeats after each cycle of cylinder oscillation. Subsequently, Khalak & Williamson (1999) defined lock-in as the matching of the frequency of the periodic wake vortex mode and the oscillation frequency of the body. This is in line with the definition used by Sarpkaya (1995) where the force frequency matches the oscillation frequency of the structure in the lock-in regime.

As is the case at large Re, computational studies in the laminar regime and $m^* = 10$ (Singh & Mittal 2005; Prasanth & Mittal 2008; Prasanth, Premchandran & Mittal 2011; Navrose *et al.* 2014) show that the frequency of cylinder oscillation and vortex shedding are identical in the lock-in regime. They are quite close to the natural frequency of the oscillator in vacuum. Outside the lock-in regime, the cylinder exhibits very low amplitude oscillations at a frequency that is nearly equal to the vortex shedding frequency of flow past a stationary cylinder. The present study is confined to the laminar flow regime. The lock-in regime is identified using the

https://doi.org/10.1017/jfm.2016.157 Published online by Cambridge University Press

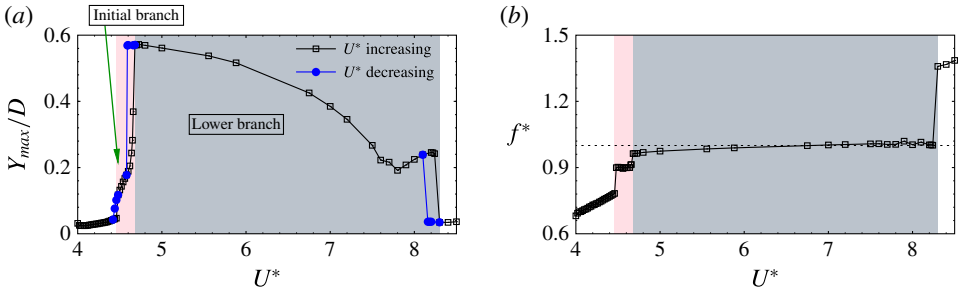

FIGURE 1. (Colour online) Flow past a freely vibrating cylinder for $Re = 100$ and $m^* = 10$: variation of (*a*) normalized maximum amplitude of cylinder oscillation, and (*b*) frequency ratio, f^*, with reduced velocity. f^* is the ratio between the cylinder vibration frequency and the natural frequency of the oscillator in vacuum. Results are shown for the computations when U^* is increased in small increments as well as when it is decreased in small decrements. The lock-in regime obtained via the increasing U^* approach is shaded: initial branch (magenta) and lower branch (grey). Hysteresis is shown only in (*a*), and not in (*b*) to avoid clutter.

metrics that have been proposed and utilized in the earlier studies: relatively high amplitude of cylinder oscillation and, matching of the cylinder oscillation and vortex shedding frequency. Figure 1 shows the amplitude of vibration and frequency ratio of a cylinder exhibiting VIV for $(Re, m^*) = (100, 10)$. The lock-in regime is highlighted via shading.

There have been relatively fewer studies that investigate the mechanism(s) underlying the lock-in phenomenon in free vibrations, i.e. what causes lock-in in free vibrations? Cossu & Morino (2000) carried out linear stability analysis for the flow past an elastically mounted cylinder in the laminar flow regime. They identified two modes that may be responsible for the onset of instability in the fluid–structure system and referred to them as the von Kármán and nearly structural modes. It was demonstrated that vortex shedding accompanied with a large amplitude of cylinder oscillation is possible for subcritical Re and low m^* owing to the instability of the nearly structural mode. Meliga & Chomaz (2011), using asymptotic analysis, corroborated the existence of the two modes reported by Cossu & Morino (2000) and renamed them the wake mode (WM) and structure mode (SM), respectively. The identification of the modes is based on their characteristics in the limit of very large mass ratio. For large m^*, the eigenvalue of the SM tends to the natural eigenvalue of the cylinder-only system. On the other hand, the eigenvalue of WM, in the limit of large m^*, tends to the leading eigenvalue computed for the flow past a stationary cylinder. Therefore, to identify the two modes for a given value of Re and reduced speed (U^*), the eigenvalue of the modes need to be followed up to large values of m^*. For certain combinations of Re and U^*, the eigenvalues may coalesce at a mass ratio. Naturally, in this situation the classification of modes as wake and structure mode is not possible. Meliga & Chomaz (2011) also carried out an approximate nonlinear analysis in the regime of linear instability of the fluid–structure system and proposed a criterion based on the amplitude of cylinder oscillation to identify the lock-in regime.

Recently, Zhang *et al.* (2015), carried out linear stability analysis of the fluid–structure system utilizing a reduced-order model for the wake. They suggested that at $Re = 60$, lock-in may result either from the instability of WM only or both WM

https://doi.org/10.1017/jfm.2016.157 Published online by Cambridge University Press

and SM. They proposed that in the first situation, lock-in occurs because of the vicinity of the frequency of WM to the natural frequency of the oscillator. This kind of lock-in was referred to as resonance-induced lock-in. In the other case, instability results from the interaction of SM and WM. This was referred to as flutter-induced lock-in. The criterion used for the identification of lock-in by Zhang *et al.* (2015) is based entirely on frequency considerations. However, it has been well established in earlier studies (for example, Govardhan & Williamson 2000) that, the frequency of the fluid–structure system in the lock-in regime may depend significantly on the mass ratio. In fact, at low enough mass ratio, the cylinder can vibrate with large oscillation amplitude and frequency that can be several times the natural frequency of the oscillator (Govardhan & Williamson 2002). Therefore, a criteria for lock-in that is based on frequency only may not be suitable for systems with moderate to low value of mass ratio.

In the present study we investigate the phenomenon of lock-in via linear stability analysis (LSA) and direct time integration (DTI) of the equations that govern the flow and response of the structure. No empirical model is used. Most of the earlier studies that explore lock-in consider variation with reduced speed while holding mass ratio fixed. The present analysis is carried out over a relatively wide range of m^* and Re, including the subcritical and supercritical regimes with respect to onset of vortex shedding. Using these results, a classification of the modes is presented. It is observed that, for large mass ratios, the modes corresponding to the two leading eigenvalues are quite distinct and maintain this distinction as U^* is varied. In this sense, the two leading modes are decoupled from each other. We refer to the two eigenmodes as the fluid mode (FM) and elastic mode (EM). The FM resembles the mode corresponding to the leading eigenvalue of the flow past a stationary cylinder. For low mass ratios, the two leading eigenmodes do not exhibit a clear distinction in terms of their affiliation to being either class fluid or class elastic. We refer to them as coupled modes.

The linear instability of the coupled fluid–structure system results in free vibrations. Depending on the operational parameters (m^*, U^*, Re) there may be several unstable modes. As the amplitude of vibration increases, nonlinear terms become significant and the response of the system is altered from its linear behaviour. As a consequence, the fluid–structure system achieves a limit cycle. However, not all unstable eigenmodes lead to high amplitude response of the cylinder. Only those unstable eigenmodes whose E_r a higher than a certain threshold value lead to lock-in. We also study the phase angle between the cylinder displacement and lift force corresponding to an eigenmode. The phase angle is found to be related to the direction of energy transfer between the fluid and structure. DTI is initiated with the disturbance field corresponding to the unstable eigenmodes. The phase angle undergoes a change as the amplitude of cylinder vibration increases.

2. The governing equations

2.1. *Incompressible flow equations*

To investigate the interaction between the fluid and the oscillating cylinder, linear stability analysis of the governing equations is carried out in a moving frame attached to the cylinder. Such an approach has been used earlier to study vortex-induced vibration of a cylinder (Étienne & Pelletier 2012; Lu & Papadakis 2014). Let $\boldsymbol{x}$ and t denote the spatial and temporal coordinates respectively. The spatial domain is represented by $\Omega \subset \mathbb{R}^2$. Γ represents the boundary of Ω. The temporal domain is

https://doi.org/10.1017/jfm.2016.157 Published online by Cambridge University Press

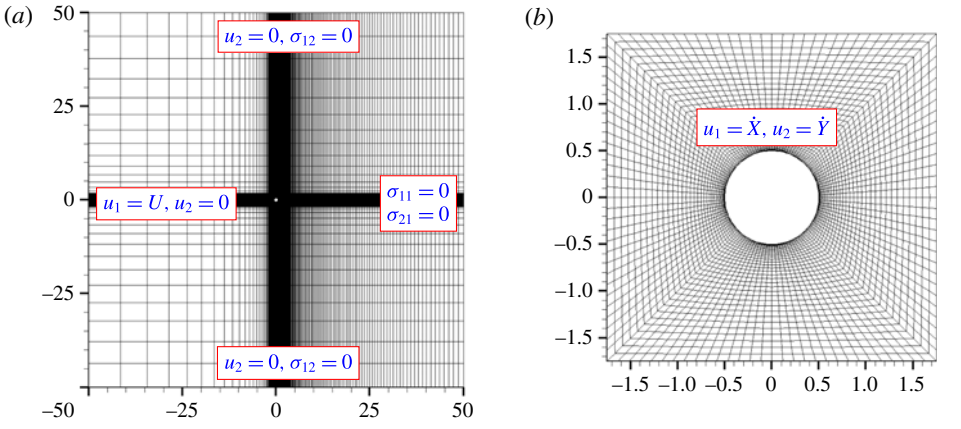

FIGURE 2. (Colour online) Flow past a freely vibrating cylinder: (*a*) finite element mesh that has been employed for the computations in this work, (*b*) close-up view of the mesh near the surface of the cylinder. The mesh consists of 12 814 nodes and 12 540 quadrilateral elements. The location of the various boundaries and boundary conditions are also shown.

represented by $(0, T)$. The Navier–Stokes equations governing an incompressible flow in the absence of body forces are

$$\rho\left(\frac{\partial \boldsymbol{u}}{\partial t} + \boldsymbol{u}\cdot\boldsymbol{\nabla}\boldsymbol{u} + \dot{\boldsymbol{U}}_b\right) - \boldsymbol{\nabla}\cdot\boldsymbol{\sigma} = \boldsymbol{0} \quad \text{on } \Omega \times (0, T), \tag{2.1}$$

$$\boldsymbol{\nabla}\cdot\boldsymbol{u} = 0 \quad \text{on } \Omega \times (0, T). \tag{2.2}$$

Here, ρ, $\boldsymbol{u}$ and $\boldsymbol{\sigma}$ are the density, velocity and stress tensor, respectively. $\boldsymbol{U}_b$ denotes the instantaneous velocity of the cylinder. For a Newtonian fluid the stress tensor is given as $\boldsymbol{\sigma} = -p\boldsymbol{I} + 2\mu\boldsymbol{\varepsilon}(\boldsymbol{u})$, where, $\boldsymbol{\varepsilon}$ is the strain rate given as $\boldsymbol{\varepsilon}(\boldsymbol{u}) = ((\boldsymbol{\nabla}\boldsymbol{u}) + (\boldsymbol{\nabla}\boldsymbol{u})^{\mathrm{T}})/2$ and, p and μ are the pressure and coefficient of dynamic viscosity, respectively.

Unlike the LSA, the DTI of the governing equations is carried out in an inertial frame of reference. Therefore, the third term in (2.1) is dropped. More details on the same can be found in our earlier work (Prasanth & Mittal 2008). The computational domain along with the boundary conditions are shown in figure 2. No-slip condition is applied on the velocity at the surface of the cylinder. The location of the cylinder and its velocity are updated at each nonlinear iteration of the solution to the flow equations.

2.2. *The equations of motion for the structure*

The motion of the cylinder mounted on elastic supports, in the two directions along the Cartesian axes, is governed by the following system of equations:

$$\dot{\boldsymbol{U}}_b + 4\pi F_N \zeta \boldsymbol{U}_b + (2\pi F_N)^2 \boldsymbol{X} = \frac{2\boldsymbol{C}_F}{\pi m^*} \quad \text{for } (0, T), \tag{2.3}$$

$$\dot{\boldsymbol{X}} = \boldsymbol{U}_b \quad \text{for } (0, T). \tag{2.4}$$

https://doi.org/10.1017/jfm.2016.157 Published online by Cambridge University Press

Here, F_N is the reduced natural frequency of the oscillator, ζ the structural damping ratio and m^* the non-dimensional mass of the body. $\boldsymbol{C_F}$ is the instantaneous coefficient of fluid force acting on the cylinder. The fluid force is computed by integrating stress on the boundary of the cylinder. $\boldsymbol{X}$ denotes the normalized displacement. The displacement and velocity are normalized by the diameter of the cylinder, D, and the free-stream speed U, respectively. F_N is related to the natural frequency of the spring mass system (f_N) as $F_N = f_N D/U$. Another related parameter is the reduced velocity, U^*. It is defined as $U^* = U/(f_N D) = 1/F_N$. Although the formulation presented here is general, results are presented for transverse-only oscillation of the structure.

2.3. *Global LSA*

We carry out a global linear stability analysis of the fluid–structure system represented by (2.1)–(2.4). A similar approach was employed by Cossu & Morino (2000). The unsteady flow variables, $(\boldsymbol{u}, p)$ are decomposed as a combination of the steady and the disturbance field: $\boldsymbol{u} = \boldsymbol{U} + \boldsymbol{u}'$ and $p = P + p'$. $(\boldsymbol{U}, P)$, the steady flow past a stationary cylinder, is obtained by dropping the unsteady terms in (2.1) and (2.2). $\boldsymbol{u}'$ and p' are the perturbation fields of the velocity and pressure, respectively. In the steady state the cylinder is at rest at its equilibrium position. Therefore, $\boldsymbol{U}_b$ is also the disturbance in the velocity of the cylinder. In the equilibrium state, the spring is in a stretched position, $\boldsymbol{X_{eq}}$, due to the steady force acting on the cylinder. In general, for a circular cylinder in uniform flow, this force is along the streamwise direction. The displacement of the cylinder, therefore, can be decomposed as $\boldsymbol{X} = \boldsymbol{X_{eq}} + \boldsymbol{x}'$, where $\boldsymbol{x}'$ represents the disturbance field of the cylinder displacement. Substituting for the decomposition of flow and the structural variables in (2.1)–(2.4), and subtracting from them, the equations for steady flow, the equations for the evolution of the disturbance field can be obtained. We assume that the disturbances are small and drop the nonlinear terms. We also assume that the system is devoid of any structural damping. This leads to the following linearized equations of the disturbance field:

$$\rho\left(\frac{\partial \boldsymbol{u}'}{\partial t} + \boldsymbol{u}' \cdot \nabla \boldsymbol{U} + \boldsymbol{U} \cdot \nabla \boldsymbol{u}' + \dot{\boldsymbol{U}}_b\right) - \nabla \cdot \boldsymbol{\sigma}' = \boldsymbol{0}, \tag{2.5}$$

$$\nabla \cdot \boldsymbol{u}' = 0, \tag{2.6}$$

$$\dot{\boldsymbol{U}}_b + (2\pi F_N)^2 \boldsymbol{x}' = \frac{2\left(\dfrac{\partial \boldsymbol{C_F}}{\partial \boldsymbol{U_b}} \cdot \boldsymbol{U_b} + \dfrac{\partial \boldsymbol{C_F}}{\partial p'} p'\right)}{\pi m^*}, \tag{2.7}$$

$$\dot{\boldsymbol{x}}' = \boldsymbol{U_b}. \tag{2.8}$$

In the equation above, $\boldsymbol{\sigma}'$ represents the stress tensor due to disturbance field of the flow. The variation in non-dimensional forces because of change in the velocity of the cylinder with respect to the equilibrium state is denoted by the matrix $\partial \boldsymbol{C_F}/\partial \boldsymbol{U_b}$. Similarly, the variation in forces because of the change in the pressure on the surface of the cylinder is $\partial \boldsymbol{C_F}/\partial p'$. For conducting the global LSA of the combined fluid–cylinder system, we assume the disturbance field of the following form:

$$\boldsymbol{u}'(\boldsymbol{x}, t) = \hat{\boldsymbol{u}}(\boldsymbol{x})\mathrm{e}^{\lambda t}, \quad p'(\boldsymbol{x}, t) = \hat{p}(\boldsymbol{x})\mathrm{e}^{\lambda t}, \quad \boldsymbol{U_b} = \hat{\boldsymbol{U}}_b \mathrm{e}^{\lambda t}, \quad \boldsymbol{x}' = \hat{\boldsymbol{x}}\mathrm{e}^{\lambda t}. \tag{2.9a–d}$$

Substituting this form of the disturbance in (2.5)–(2.8) we obtain:

$$\rho(\lambda(\hat{\boldsymbol{u}} + \hat{\boldsymbol{U}}_b) + \hat{\boldsymbol{u}} \cdot \nabla \boldsymbol{U} + \boldsymbol{U} \cdot \nabla \hat{\boldsymbol{u}}) - \nabla \cdot \hat{\boldsymbol{\sigma}} = 0, \tag{2.10}$$

https://doi.org/10.1017/jfm.2016.157 Published online by Cambridge University Press

$$\nabla \cdot \hat{\boldsymbol{u}} = 0, \tag{2.11}$$

$$\lambda \hat{\boldsymbol{U}}_b + (2\pi F_N)^2 \hat{\boldsymbol{x}} = \frac{2\left(\dfrac{\partial \boldsymbol{C_F}}{\partial \hat{\boldsymbol{U}}_b} \cdot \hat{\boldsymbol{U}}_b + \dfrac{\partial \boldsymbol{C_F}}{\partial \hat{p}} p'\right)}{\pi m^*}, \tag{2.12}$$

$$\lambda \hat{\boldsymbol{x}} = \hat{\boldsymbol{U}}_b. \tag{2.13}$$

Here, λ is the eigenvalue of the coupled fluid–structure system and governs its stability. In general, $\lambda = \lambda_r + \mathrm{i}\lambda_i$, where λ_r and λ_i are the real and imaginary parts, respectively. We define the non-dimensional frequency of the eigenmode as $F_{LSA} = \lambda_i/2\pi$. The corresponding reduced velocity is represented by $U^*_{LSA} = 2\pi/\lambda_i = 1/F_{LSA}$. In this study, we restrict the motion of the cylinder in the direction transverse to the free-stream flow. This is commonly referred to as Y-only oscillations. A typical global eigenmode of the fluid–structure system is thus represented as $(\hat{\boldsymbol{u}}(\boldsymbol{x}), \hat{p}(\boldsymbol{x}), \hat{\hat{Y}}, \hat{Y})$.

3. The finite element formulation

A stabilized finite element method has been utilized to carry out the time integration of the governing equations as well as their linear stability analyses. The numerical stabilizations are based on SUPG (streamline-upwind/Petrov–Galerkin) and PSPG (pressure-stabilizing/Petrov–Galerkin) techniques (Tezduyar *et al.* 1992*c*). All the stabilizations used in this work are residual based. Therefore, they lead to a consistent formulation in the sense that the exact solution satisfies the finite element formulation. The steady state about which stability analysis is carried out is obtained by simply dropping the unsteady term in the governing equations. For carrying out direct time integration, a space–time version of the stabilized finite element method is employed (Tezduyar *et al.* 1992*a*; Tezduyar, Liou & Behr 1992*b*). We rewrite (2.1) and (2.2) in the stationary frame. The equations of motion for the oscillator are also cast in the space–time formulation as described in the articles by Mittal & Tezduyar (1992*a*,*b*) and Tezduyar *et al.* (1992*c*). This method allows us to carry out computations that involve moving boundaries and interfaces. The finite element mesh that has been employed for all the computations is shown in figure 2.

The finite element formulation of the linear stability analysis of flow equations is the extension of that presented in our earlier studies (Mittal & Kumar 2007; Mittal & Verma 2014). The stabilization coefficients for the formulation are based on the steady-state velocity field, $\boldsymbol{U}^h$. In this work the formulation is extended to include (2.12) and (2.13) for the structure. The finite element discretization of (2.10)–(2.13) leads to a generalized eigenvalue problem of the form $\boldsymbol{A}X - \lambda \boldsymbol{B}X = 0$, where $\boldsymbol{A}$ and $\boldsymbol{B}$ are non-symmetric matrices. We use a shift-invert transformation in conjunction with the subspace iteration method to track the fastest growing eigenmodes. The growth rate of the eigenmodes obtained from LSA is confirmed by tracking the growth rate of the energy of the disturbance from the DTI of the governing equations. This is illustrated for a few cases in § 8 by initiating computations with the eigenmodes obtained from LSA.

4. Eigenmodes from the linear stability analysis

4.1. *Classification of modes*

Compared to the fluid alone, LSA of the fluid–structure model is associated with two additional eigenmodes. Cossu & Morino (2000) and Meliga & Chomaz (2011)

https://doi.org/10.1017/jfm.2016.157 Published online by Cambridge University Press

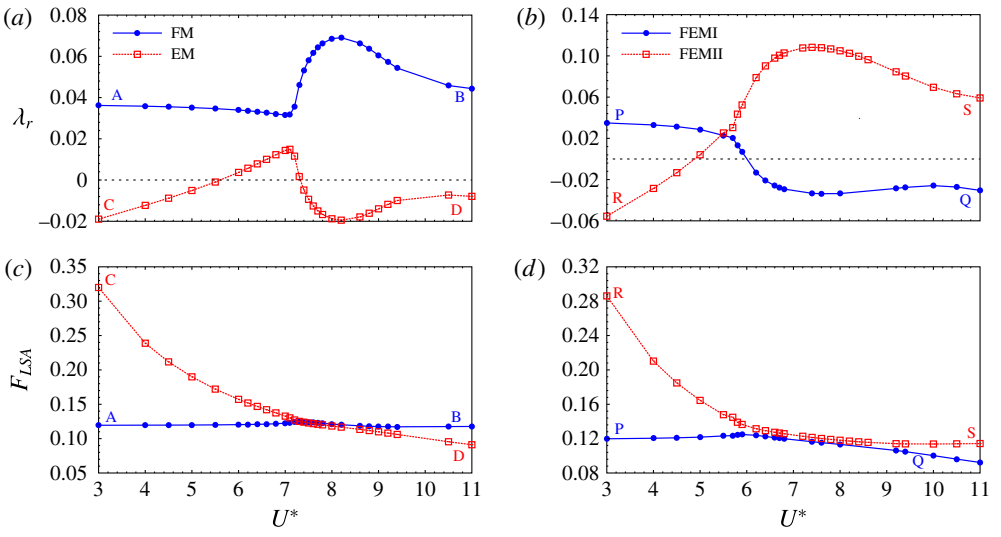

FIGURE 3. (Colour online) Linear stability analysis of the steady flow past a fluid–structure system: stability characteristics for (*a*,*c*) $(Re, m^*) = (60, 20)$, (*b*,*d*) $(Re, m^*) = (60, 5)$. λ_r represents the growth rate and $F_{LSA} = \lambda_i/2\pi$ represents the non-dimensional frequency.

presented a classification of the eigenmodes based on their characteristics in the limit of very large m^*. To identify the class to which an eigenmode belongs for a given value of Re and U^*, the eigenvalue has to be followed up to large values of m^*. Most studies on VIV that explore the characteristics of the fluid–structure system in lock-in regime consider its variation with reduced speed while holding the mass ratio fixed. A different perspective towards mode classification is adopted in this work wherein m^* is fixed and the eigenmodes are computed over a wide range of U^*. The present classification makes it relatively easier to compare the characteristics of fluid–structure system in the lock-in regime with the properties of the unstable modes. It is observed that for systems with large m^*, the modes corresponding to two leading eigenvalues are quite distinct and maintain this distinction for all U^*. That is, in terms of variation with U^*, the two leading eigenmodes are decoupled. We refer to the two modes as fluid mode and elastic mode. The frequency of FM remains nearly constant with U^*. The frequency of EM, on the other hand, varies inversely with U^*. For low m^*, the two leading eigenmodes do not exhibit a clear distinction in terms of their affiliation to being either class elastic or class fluid. We refer to such modes as coupled modes and denote them by fluid–elastic mode I (FEMI) and fluid–elastic mode II (FEMII). For small U^*, FEMI resembles fluid mode and FEMII is similar to elastic mode. However, for large U^*, the characteristics of FEMI and FEMII resemble EM and FM respectively. A detailed description of decoupled and coupled modes for the $Re = 60$ flow is presented for two values of mass ratio, $m^* = 20$ and 5. The modes are decoupled for $m^* = 20$, while they are coupled for $m^* = 5$. In the discussion that follows, we refer to the mode responsible for the onset of global instability in the flow past a stationary cylinder as the stationary wake mode.

Figure 3(*a*) shows the variation of the growth rate of the fluid and the elastic mode with U^* for $(Re, m^*) = (60, 20)$. The fluid mode is unstable for all U^*. It achieves maximum growth rate for $U^* = 8.0$. The growth rate of FM approaches the

https://doi.org/10.1017/jfm.2016.157 Published online by Cambridge University Press

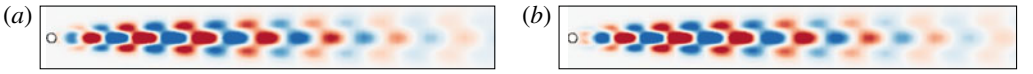

FIGURE 4. (Colour online) Linear stability analysis of the $Re = 60$ steady flow past a circular cylinder: vorticity field for the (*a*) real and (*b*) imaginary parts of the eigenmode corresponding to the stationary wake mode. The flow is from left to right.

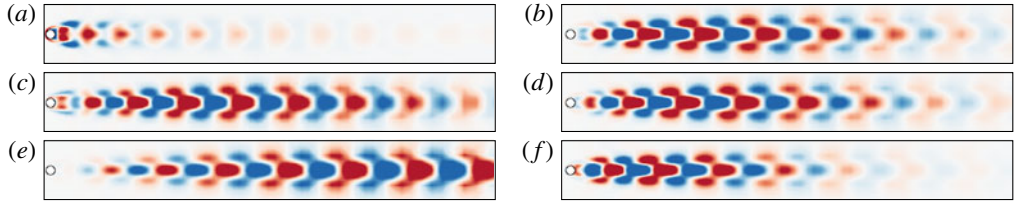

FIGURE 5. (Colour online) Linear stability analysis of the steady flow past a fluid–structure system for $(Re, m^*) = (60, 20)$: spanwise vorticity field of the EM (*a*,*c*,*e*) and the FM (*b*,*d*,*f*) for (*a*,*b*) $U^* = 5.5$, (*c*,*d*) $U^* = 7.0$ and (*e*,*f*) $U^* = 8.0$. The flow is from left to right.

growth rate of the stationary wake mode for $Re = 60$ for very small and very large values of U^*. The elastic mode is unstable for $5.8 < U^* < 7.3$. This mode attains highest growth rate for $U^* = 7.0$. Figure 3(*c*) shows the variation of non-dimensional frequency, $F_{LSA} = \lambda_i/2\pi$, with U^*. The frequency of the fluid mode remains close to the frequency of the stationary wake mode for all U^*. It is noted that the growth rate of both modes achieve maximum within the range of U^* where the frequencies of the two modes are close to each other. Figure 4 shows the vorticity field for the real and imaginary parts of the unstable eigenmode for the steady flow past a stationary cylinder at $Re = 60$. Figure 5 shows the vorticity field for FM and EM for different U^* at $(Re, m^*) = (60, 20)$. It is observed that the shape of the eigenmode is closely related to its frequency (F_{LSA}). If the frequency associated with the eigenmode is relatively larger, then the region of large perturbation associated with the mode is closer to the cylinder. As the frequency of the eigenmode decreases, the large perturbation region shifts downstream with respect to the cylinder. The frequency of FM remains close to that of the $Re = 60$ stationary wake mode for all values of U^*. Therefore, the mode shape of FM resembles the stationary wake mode (figure 4) for all reduced speeds. On the other hand, the frequency of EM follows the natural frequency of the structure-only system over a wide range of U^*. As a result, with increase in U^* the region of large perturbation associated with EM moves downstream to the cylinder. For U^* values where the frequency of FM and EM are close to each other, no perceptible difference is observed in the structure of the two modes.

Figure 3(*b*,*d*) shows the stability characteristics of FEMI and FEMII for $(Re, m^*) = (60, 5)$. The vorticity field of the eigenmodes for different values of U^* are shown in figure 6. The growth rate, frequency and mode shape of FEMI resemble the stationary wake mode for low U^*. In the same U^* regime, FEMII is stable and its frequency follows the structure-only system. Concomitantly, the region of large perturbation associated with FEMII moves downstream to the cylinder with increase in reduced speed. The growth rate of FEMI decreases with increase in U^* and the mode becomes stable beyond $U^* = 6.0$. FEMII is unstable for $U^* \geqslant 5.0$. Towards the higher-U^* end, growth rate, frequency and mode shape of FEMII resemble the stationary wake mode.

https://doi.org/10.1017/jfm.2016.157 Published online by Cambridge University Press

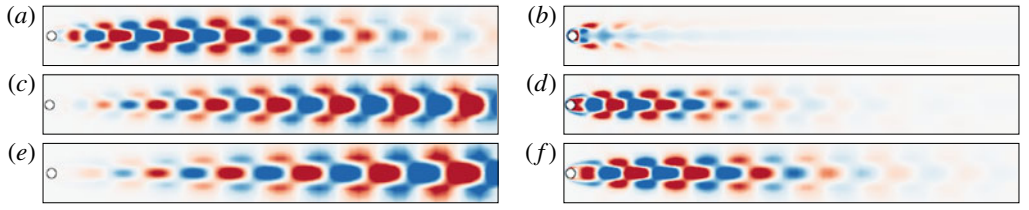

FIGURE 6. (Colour online) Linear stability analysis of the steady flow past a fluid–structure system for $(Re, m^*) = (60, 5)$: spanwise vorticity field of FEMI (a,c,e) and FEMII (b,d,f) for (a,b) $U^* = 4.0$, (c,d) $U^* = 6.8$ and (e,f) $U^* = 10.0$. The flow is from left to right.

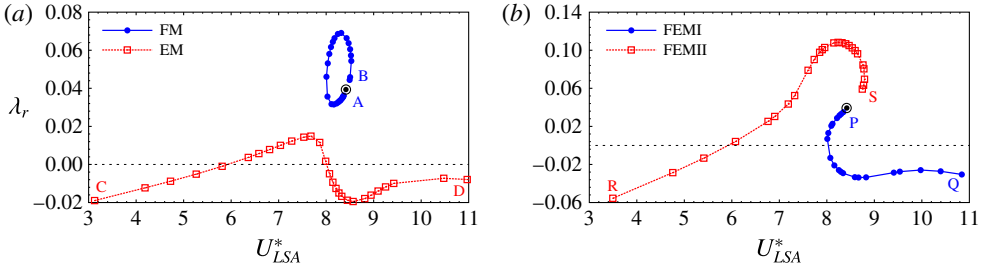

FIGURE 7. (Colour online) Linear stability analysis of the steady flow past a fluid–structure system: variation of $U^*_{LSA} = 2\pi/\lambda_i = 1/F$ with U^* for (a) $(Re, m^*) = (60, 20)$ and (b) $(Re, m^*) = (60, 5)$. The point corresponding to stationary wake mode is shown in bull's eye symbol.

For FEMI, at large values of U^*, the large perturbation region associated with the eigenmode moves downstream with increase in U^*. For $6.0 \leqslant U^* \leqslant 9.0$, the frequencies of the two modes are close to each other and their variations with U^* are also similar. The growth rate of the unstable FEMII achieves maximum within this range.

To further bring out the distinction between the coupled and decoupled modes we replot the results shown in figure 3 on the λ_r–U^*_{LSA} plane; $U^*_{LSA}(= 1/F_{LSA})$ is the reduced velocity based on the frequency of the eigenmode. Figure 7 shows the variation of the growth rate with U^*_{LSA} for $(Re, m^*) = (60, 20)$ and $(60, 5)$. The end points of the curves are tagged with A–B for FM, C–D for EM, P–Q for FEMI and R–S for FEMII. The location of these points in figure 3 is also marked. In the case of decoupled modes, the end points of the fluid mode, at the low (point A) and high end of U^* (point B), approach each other with increase in the range of U^*. For the limiting case when the reduced velocity spans from zero to infinity, FM would appear as a closed ring, separate from EM, on λ_r–U^*_{LSA} plane. The point where the end points of the ring merge, corresponds to that for the stationary wake mode (shown as bull's eye symbol in figure 3). For the case of coupled modes, with increase in the range of U^*, the end point of FEMII (point S) and the beginning of FEMI (point P) approach the point corresponding to the stationary wake mode. In the limiting case when the reduced velocity spans from zero to infinity, the two modes would merge at the point corresponding to stationary wake mode on λ_r–U^*_{LSA} plane and appear as a single curve. Figure 7 clearly brings out the distinction between the coupled and decoupled modes and the identification of the two branches.

https://doi.org/10.1017/jfm.2016.157 Published online by Cambridge University Press

4.2. Regime of coupled and decoupled modes

In general, whether the modes are coupled or decoupled depends on m^* and Re. At a given Re, the modes are coupled for relatively low m^* and get decoupled to EM and FM at larger m^*. We define critical mass ratio, m_c^*, as the largest mass ratio for which modes are coupled at a certain Re. We also define Re_o as the Reynolds number beyond which the stationary wake mode becomes unstable. The value of Re_o estimated with the mesh employed in the present study is $Re_o = 47.5$. The value of Re_o from the study reported by Kumar & Mittal (2006), independent of mesh and blockage effects, is $Re_o = 47$. The two values are in very good agreement. The small difference between the two studies is attributed to the slightly lower spatial resolution in the present study. Compared to the flow past stationary cylinder, the coupled fluid–structure system has additional degrees of freedom corresponding to cylinder displacement and velocity. In addition, these degrees of freedom are strongly coupled with the flow variables at the surface of the cylinder. Therefore, LSA of the coupled fluid–structure problem is relatively more demanding on computational resources as compared to the fluid-only and structure-only problems. One of the factors in choosing the finite element mesh used in the present study is that with the computational resources at our disposal, we should be able to carry out LSA over a wide range of the various parameters of interest (Re, U^*, m^*). A mesh convergence study is carried out to check the adequacy of the mesh against a mesh of finer spatial resolution. The details of the mesh convergence study are presented in appendix A. The results from the two meshes are found to be in very good agreement. The effect of m^* on (de-)coupling of modes is presented with Re. To account for the offset in the value of Re_o compared to that reported by Kumar & Mittal (2006), we additionally present the results with respect to Re/Re_o. Marais *et al.* (2011) used a similar approach to present their results on stability analysis. They recorded a value of $Re_o = 64$ in their experiments because of confinement and blockage effects.

Figure 8(*a*) shows the regions in Re–m^* plane where the modes are coupled or decoupled. We describe the procedure used to generate this figure. For several values of Re, computations are carried out for many values of m^* that are separated by a step size of $\Delta m^* = 5.0$. At each of these (Re, m^*) values, LSA is carried out over a wide range of reduced speed. The variation of λ_r with U^*_{LSA} is utilized to identify coupled/decoupled modes. In the range of m^* where the system transits between coupled and decoupled modes, computations are carried out for more m^* values that are separated by a finer step size of $\Delta m^* = 1.0$. These are utilized to estimate the critical mass ratio, m_c^*, beyond which the modes are decoupled for a given Re. These values are shown in figure 8(*a*) by solid circles. We note that m_c^* decreases as one moves away from Re_o. Figure 8(*b–d*) shows the variation of λ_r with U^*_{LSA} for $m^* = 75$ at $Re = 37.5$, 47 and 56.5, respectively. For $Re = 37.5$ and 56.5 the modes are decoupled. While the fluid mode is stable for former, it is unstable in the latter case. For $Re = 47.0$ ($Re/Re_o = 1.0$), the modes are coupled. The value of λ_r at the junction, where the branches corresponding to modes FEMI and FEMII meet, is equal to zero. The transition from the regime of coupled modes to decoupled modes with increase in mass ratio is demonstrated in figure 9 for $Re = 42$ and 52 by the evolution of the topology of the curves.

The term critical mass ratio has been used in earlier studies on free vibrations in different contexts. For example, Govardhan & Williamson (2000) introduced a critical mass ratio, m^*_{crit}, below which synchronization is observed for values of U^* up to infinity. Prasanth *et al.* (2011) introduced a critical mass ratio, m^*_{cr}, below which hysteresis between the initial and lower branch, at low Re and in an unbounded

https://doi.org/10.1017/jfm.2016.157 Published online by Cambridge University Press

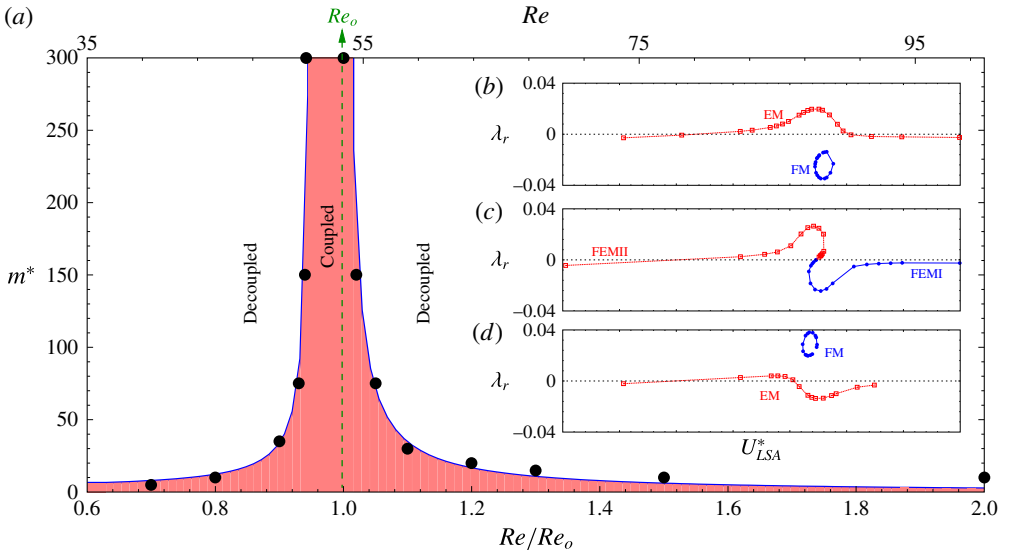

FIGURE 8. (Colour online) Linear stability analysis of the steady flow past a fluid–cylinder system: (*a*) the regions of mode coupling/decoupling. The variation of growth rate of modes with U^*_{LSA} for $m^* = 75$ at (*b*) $Re = 37.5$, (*c*) $Re = Re_o = 47$ and (*d*) $Re = 56.5$.

domain, disappears. The term critical mass ratio, in the present work, is not related to these two phenomena. In the following sections most of the results and figures are presented for the case of coupled modes. The general argument can be extended to the case of coupled modes as well.

5. Lock-in regime

As a first step towards exploring the connection between the lock-in phenomenon and linear instability of the fluid–structure system, we identify the lock-in regime in the cylinder response obtained from the DTI of governing equations. Later in the section, we present a comparison of the lock-in regime obtained from DTI with that estimated from the results of LSA. In the linear regime the fluid and the structure system are associated with the same growth rate and frequency (2.9). A positive growth rate, via linear theory, would necessarily lead to very large oscillations of the fluid–structure system at sufficiently large times. Therefore, it is appropriate to conclude that in the linear regime, instability is synonymous with lock-in/synchronization. However, as the disturbance field becomes large the nonlinear terms in the governing equations become significant; the system can no longer be approximated by dropping the nonlinear effects. In fact, the nonlinear terms drive the system to a limit cycle with finite amplitude of oscillation and with modified frequency. This may change the lock-in range as compared to that predicted by LSA. Figures 10–12 show the lock-in regime predicted by LSA and DTI of the governing equations. The results shown for DTI are the ones when the oscillations have reached a limit cycle. The three figures are discussed in detail below.

$Re \leqslant Re_o$: Figure 10(*a*,*b*) shows the variation of normalized maximum amplitude of transverse oscillation and frequency ratio with U^* for $(Re, m^*) = (40, 10)$ obtained

https://doi.org/10.1017/jfm.2016.157 Published online by Cambridge University Press

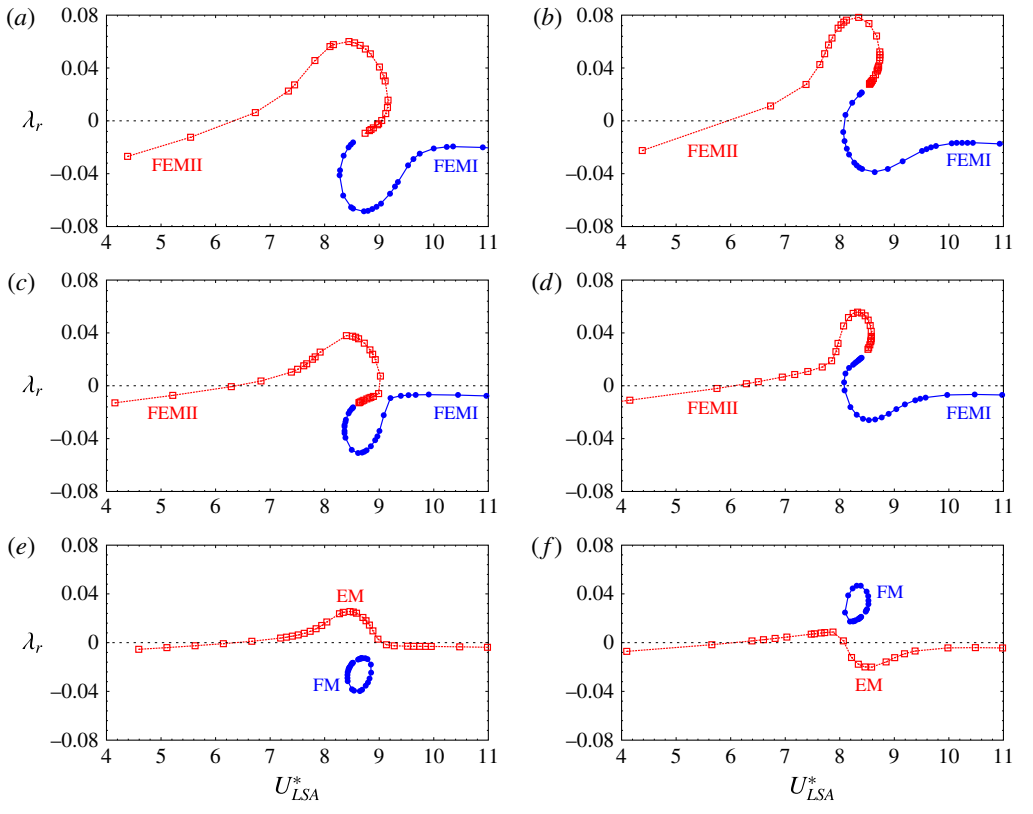

FIGURE 9. (Colour online) Linear stability analysis of the steady flow past a fluid–cylinder system: variation of growth rate with U^*_{LSA} of modes for for (*a*) $(Re, m^*) = (42, 10)$, (*c*) $(Re, m^*) = (42, 25)$, (*e*) $(Re, m^*) = (42, 50)$, (*b*) $(Re, m^*) = (52, 10)$, (*d*) $(Re, m^*) = (52, 25)$, (*f*) $(Re, m^*) = (52, 40)$.

from DTI. The frequency ratio, f^*_{DTI}, is defined as the ratio of the frequency of the cylinder oscillation to the natural frequency of the oscillator in vacuum. It is observed that lock-in/synchronization occurs for $5.9 < U^* < 10.1$. Outside this range of U^* the flow is steady and the cylinder is at rest. In the lock-in regime, the cylinder oscillations are accompanied with vortex shedding and the frequency ratio is close to unity. As shown in figure 10(*a*,*c*), LSA predicts instability of the fluid–structure system in exactly the same regime of U^* as computed from DTI. The instability sets in via the elastic mode. We note that the fluid mode is stable for all U^* for subcritical Re. The frequency ratio, $f^*_{LSA} = \lambda_i/(2\pi F_N)$, of EM is also close to unity as is f^*_{DTI}. However, the two values are different (figure 10*c*,*d*). The difference is attributed to nonlinear effects that are associated with DTI. The effect of nonlinearities on the frequency response of the fluid–structure system has been explored by Meliga & Chomaz (2011) for systems with relatively large mass ratio. In the scenario of coupled modes, lock-in occurs via FEMII while FEMI is stable for all U^*.

$Re > Re_o$: Figure 11(*a*,*b*) shows the variation of Y_{max}/D and f^*_{DTI} with U^* for $(Re, m^*) = (60, 20)$. The amplitude and the frequency of the cylinder response show that lock-in occurs over $5.8 < U^* < 9.3$. The cylinder exhibits large amplitude of vibration within the lock-in regime. The frequency ratio in the lock-in regime is closer to unity than

https://doi.org/10.1017/jfm.2016.157 Published online by Cambridge University Press

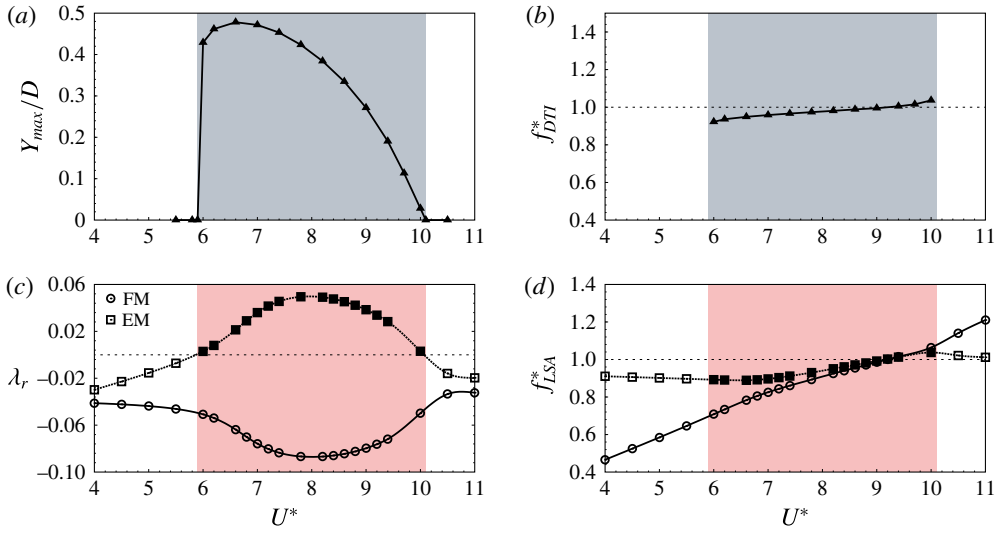

FIGURE 10. (Colour online) Flow past a fluid–cylinder system for $(Re, m^*) = (40, 10)$: variation of (a) normalized maximum amplitude of cylinder response and (b) frequency ratio with reduced velocity obtained from DTI. The lock-in regime from DTI, in the presence of nonlinear effects, is shaded in grey in (a,b). The variation of growth rate and frequency ratio of the eigenmodes with reduced velocity are shown in (c) and (d), respectively. The stable and unstable eigenmodes are denoted by hollow and solid symbols, respectively. The range of U^* over which the system is linearly unstable is shaded in (c,d).

outside the range of lock-in. LSA, in this case, shows that FM is unstable for all U^*; suggesting lock-in forever (figure 11c). The elastic mode is unstable over $5.8 < U^* < 7.3$. Figure 12(a,b) shows the variation of Y_{max}/D and f^*_{DTI} with U^* for $(Re, m^*) = (60, 5)$. In this case also the fluid–structure system is linearly unstable for all U^*. For low values of U^*, the instability occurs via FEMI while for large U^*, FEMII is unstable. The results from DTI show that lock-in for $(Re, m^*) = (60, 5)$ occurs over $5.0 < U^* < 8.8$. Compared to free vibrations at subcritical Re, the oscillations for $Re > Re_o$ are different on two major counts.

(1) The U^*-range of lock-in from DTI and LSA are different: for $Re \leqslant Re_o$, prediction of the lock-in range from LSA matches the range observed from DTI. This is not so for $Re > Re_o$. The fluid–structure system is linearly unstable for all U^*. However, nonlinear effects lead to saturation of oscillation amplitude of the cylinder to relatively low values outside the lock-in regime. More specifically, the phase between the lift and displacement as well as the frequency undergo a significant change due to the nonlinear effects leading the system to desynchronization. Desynchronization is indicated by a strong departure of f^* from unity (results for DTI in figure 11b). A question that arises from this observation is, 'Is there any feature in the unstable eigenmodes from LSA that might indicate whether it will eventually lead to lock-in or no lock-in?' We explore this in the next section by studying the relative distribution of energy in an eigenmode between the fluid and the structure.

(2) The mode that leads to synchronization: for $Re \leqslant Re_o$, only one mode is unstable and it controls the dynamics; instability sets in via EM for decoupled modes and FEMII for the case of coupled modes. However, for $Re > Re_o$, multiple

https://doi.org/10.1017/jfm.2016.157 Published online by Cambridge University Press

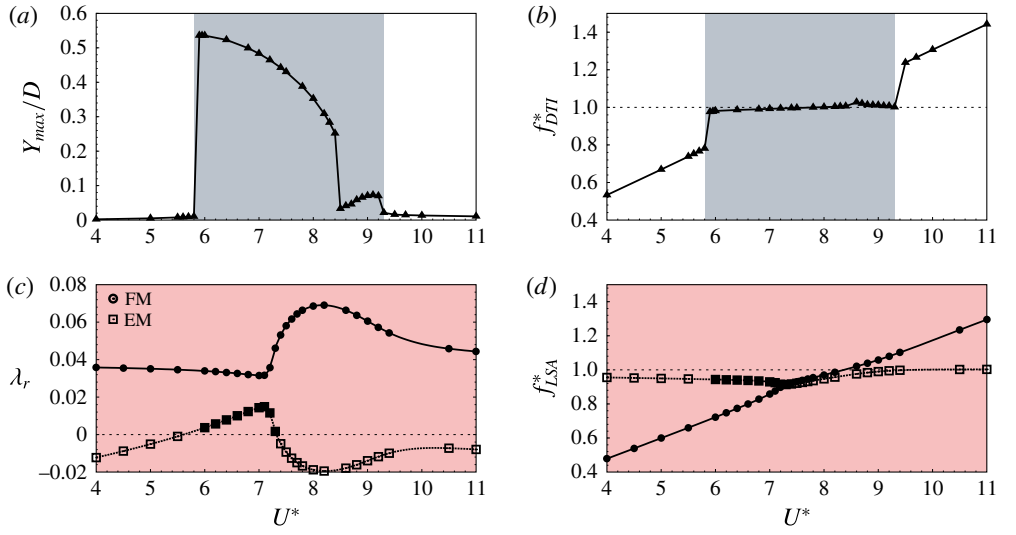

FIGURE 11. (Colour online) Flow past a fluid–cylinder system for $(Re, m^*) = (60, 20)$: variation of (*a*) normalized maximum amplitude of cylinder response and (*b*) frequency ratio with reduced velocity obtained from DTI. The lock-in regime from DTI, in the presence of nonlinear effects, is shaded in grey in (*a*,*b*). The variation of growth rate and frequency ratio of the eigenmodes with reduced velocity are shown in (*c*) and (*d*), respectively. The stable and unstable eigenmodes are denoted by hollow and solid symbols, respectively. The range of U^* over which the system is linearly unstable is shaded in (*c*,*d*).

eigenmodes may be unstable depending on the operational U^*. For $(Re, m^*) = (60, 20)$, towards the lower U^* end of lock-in, both EM and FM are unstable $(5.8 < U^* < 7.3)$. Similarly, for $(Re, m^*) = (60, 5)$, both FEMI and FEMII are unstable for $5.0 < U^* < 6.0$. In next section we explore the question as to 'which of the two modes leads to lock-in?' It is shown that for $(Re, m^*) = (60, 20)$, compared to FM, EM is associated with higher energy transfer from the fluid to the cylinder. Therefore, for $5.9 \leqslant U^* \leqslant 7.2$, the elastic mode leads to lock-in. For $7.2 < U^* \leqslant 9.2$, lock-in occurs via the fluid mode as it is the only unstable mode. In the case of coupled modes, lock-in occurs via FEMII as it is associated with higher energy transfer than FEMI.

6. Energy considerations related to eigenmodes

6.1. *Energy ratio*

We consider the disturbance field given by (2.9). In general, the eigenvalues/eigenmodes are complex. The total energy of the fluid–oscillator system associated with the disturbance field is the sum of the structural energy, E_s, and the kinetic energy of the fluid, E_f. The two components are defined as:

$$E_s(t) = \tfrac{1}{2} m^* \dot{Y}\overline{\dot{Y}} + \tfrac{1}{2}(2\pi F_n)^2 m^* Y\overline{Y}, \tag{6.1}$$

$$E_f(t) = \frac{1}{2}\int_{\Omega} \boldsymbol{u}\cdot\overline{\boldsymbol{u}}\,\mathrm{d}\Omega. \tag{6.2}$$

In (6.1) the first term on the right-hand side is the contribution of the kinetic energy of the cylinder while the second term arises from the potential energy of the spring.

https://doi.org/10.1017/jfm.2016.157 Published online by Cambridge University Press

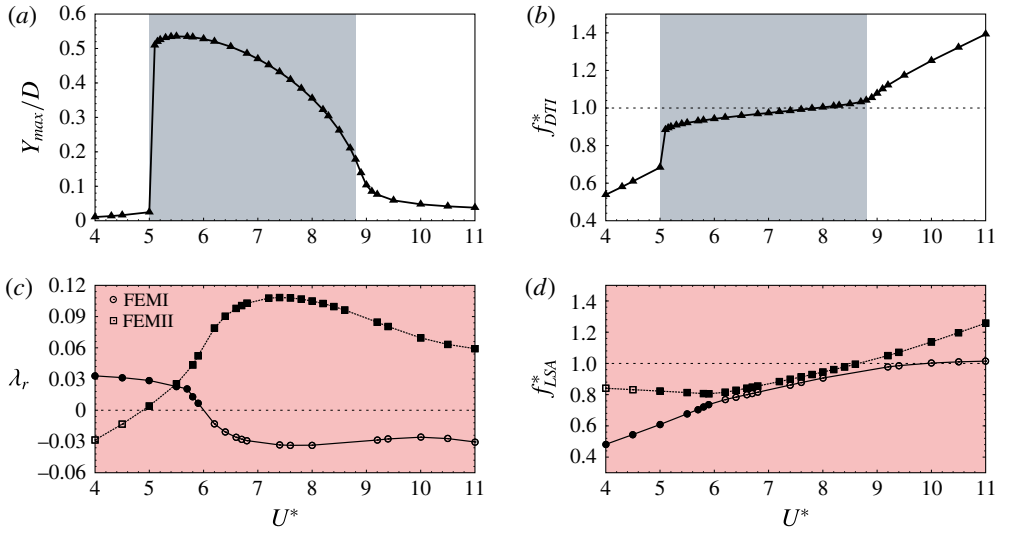

FIGURE 12. (Colour online) Flow past a fluid–cylinder system for $(Re, m^*) = (60, 5)$: variation of (a) normalized maximum amplitude of cylinder response and (b) frequency ratio with reduced velocity obtained from DTI. The lock-in regime from DTI, in the presence of nonlinear effects, is shaded in grey in (a,b). The variation of growth rate and frequency ratio of the eigenmodes with reduced velocity are shown in (c) and (d), respectively. The stable and unstable eigenmodes are denoted by hollow and solid symbols, respectively. The range of U^* over which the system is linearly unstable is shaded in (c,d).

Equations (6.1) and (6.2) can be rewritten as

$$E_s(t) = \hat{E}_s e^{2\lambda_r t}, \tag{6.3}$$

$$E_f(t) = \hat{E}_f e^{2\lambda_r t}, \tag{6.4}$$

where $\hat{E}_s$ and $\hat{E}_f$ are given as,

$$\hat{E}_s = \tfrac{1}{2} m^* \hat{\dot{Y}} \overline{\hat{\dot{Y}}} + \tfrac{1}{2} (2\pi F_n)^2 m^* \hat{Y} \overline{\hat{Y}}, \tag{6.5}$$

$$\hat{E}_f = \frac{1}{2} \int_\Omega \hat{\boldsymbol{u}} \cdot \overline{\hat{\boldsymbol{u}}} \, \mathrm{d}\Omega. \tag{6.6}$$

We define the energy ratio as $E_r = E_s(t)/(E_s(t) + E_f(t))$. It denotes the fraction of the total energy of the disturbance field contained in the structure; $(1 - E_r)$ is the fraction of the total energy of the disturbance due to the motion of the fluid. We note that E_r is constant with respect to time and can also be computed via $E_r = \hat{E}_s/(\hat{E}_s + \hat{E}_f)$. The evolution of $E_s(t)$, therefore, depends on E_r and λ_r. If λ_r is positive, E_s, grows with time. However, the nonlinear terms become significant when the disturbance field becomes relatively large. As a consequence, the fluid–structure system tends towards a limit cycle. The saturated oscillation amplitude of the spring mass oscillator significantly depends on E_r of the unstable mode. We will show later in the paper that systems with relatively large E_r, coupled with positive growth rate, attain large amplitude oscillations resulting in synchronization. The threshold

https://doi.org/10.1017/jfm.2016.157 Published online by Cambridge University Press

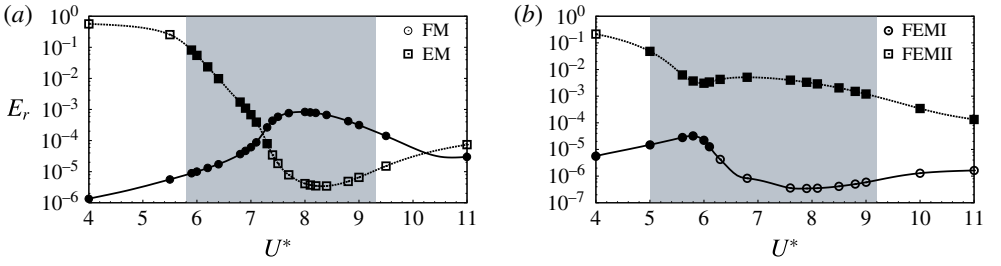

FIGURE 13. Linear stability analysis of the steady flow past a fluid–cylinder system: variation of energy ratio of the eigenmodes with U^* for (*a*) $(Re, m^*) = (60, 20)$ and (*b*) $(Re, m^*) = (60, 5)$. The stable and the unstable eigenmodes are shown as hollow and solid symbols, respectively. The lock-in regime from DTI, in the presence of nonlinear effects, is shaded in the figures.

value of E_r beyond which the unstable eigenmodes lead to lock-in state depends on Re and m^*. For example for $(Re, m^*) = (60, 20)$, all unstable eigenmodes that are associated with $E_r > 2 \times 10^{-4}$ lead to lock-in. Figure 13(*a*) shows the variation of E_r with U^* for the elastic and fluid mode for $(Re, m^*) = (60, 20)$. The same for the case of coupled modes at $(Re, m^*) = (60, 5)$ is shown in figure 13(*b*). To clearly bring out the features in the variation of E_r with U^* and the relative behaviour of the two eigenmodes, the vertical axis is shown in log scale. Also shown in the figures, via shading, is the lock-in regime obtained from DTI. The stable and the unstable eigenmodes are denoted by hollow and solid symbols, respectively. E_r of the unstable eigenmodes is relatively low outside the lock-in regime. Within the lock-in regime, for each U^*, the energy ratio of at least one unstable eigenmode has a large value. For $(Re, m^*) = (60, 20)$, EM has high E_r for U^* up to 7.3 approximately. Beyond $U^* \sim 7.3$, EM is stable and is not expected to play any role in lock-in. In this flow regime, though, E_r for the fluid mode is large and is expected to drive the system towards lock-in. For $(Re, m^*) = (60, 5)$, FEMII has a significantly large values of E_r over the entire lock-in regime. Lock-in in this case, therefore, is expected via FEMII.

6.2. *Energy transfer per oscillation cycle*

The key to self-excited nature of free vibrations is the net energy transfer over a cycle from the fluid to the oscillator (Williamson & Roshko 1988; Morse & Williamson 2009). The time evolution of cylinder displacement and lift coefficient corresponding to an eigenmode $(\hat{\boldsymbol{u}}, \hat{p}, \hat{Y}, \hat{Y})$ is given as:

$$Y(t) = \frac{(\hat{Y}e^{\lambda t} + \text{c.c.})}{2}, \tag{6.7}$$

$$C_L(t) = \frac{(\hat{C}_L e^{\lambda t} + \text{c.c.})}{2}. \tag{6.8}$$

Here, $\hat{C}_L$ is the lift coefficient calculated by integrating the stress corresponding to the eigenmode at the boundary of the cylinder. In general, $\hat{Y}$ and $\hat{C}_L$ are complex and c.c. represents the complex conjugate. Let $|\hat{Y}|$ and $|\hat{C}_L|$ represent the magnitude of

https://doi.org/10.1017/jfm.2016.157 Published online by Cambridge University Press

$\hat{Y}$ and $\hat{C}_L$, respectively. Further, let θ and $\theta + \phi$ denote the argument of $\hat{Y}$ and $\hat{C}_L$, respectively, where ϕ is the phase angle between the cylinder displacement and lift coefficient. We recall that $\lambda = \lambda_r + \mathrm{i}\lambda_i$. Equations (6.7) and (6.8) can be rearranged and written as:

$$Y(t) = Y_o(t)\mathrm{e}^{\lambda_r t}; \quad Y_o(t) = |\hat{Y}|\cos(\lambda_i t + \theta), \tag{6.9a,b}$$

$$C_L(t) = C_{L_o}(t)\mathrm{e}^{\lambda_r t}; \quad C_{L_o}(t) = |\hat{C}_L|\cos(\lambda_i t + \theta + \phi). \tag{6.10a,b}$$

The non-dimensional energy transfer from the fluid to the oscillator over a time interval, T_1–T_2 is defined as:

$$E_{transfer}(T_1, T_2) = \int_{T_1}^{T_2} C_L(t)\dot{Y}(t)\,\mathrm{d}t. \tag{6.11}$$

We now consider the non-dimensional energy transfer over a time period of cylinder oscillation from that part of C_L and Y that excludes the exponential growth/decay. The time period of cylinder oscillation is related to λ_i as $T_c = 2\pi/\lambda_i$. We define E_c, energy transfer per oscillation cycle, as:

$$E_c = \int_0^{T_c} C_{L_o}(t)\dot{Y}_o(t)\,\mathrm{d}t. \tag{6.12}$$

E_c and $E_{transfer}$ are related as

$$E_{transfer}(t, t + T_c) = E_c \int_t^{t+T_c} \mathrm{e}^{2\lambda_r t}\,\mathrm{d}t. \tag{6.13}$$

Plugging in the expressions of C_{L_o} and Y_o from (6.9) and (6.10) in (6.12), it can be shown that

$$E_c = \pi|\hat{C}_L||\hat{Y}|\sin\phi. \tag{6.14}$$

It is noted that E_c is directly proportional to $\sin\phi$. For $0° < \phi < 180°$, $E_c > 0$ and the energy transfer per cycle of oscillation is from the flow to the oscillator. In this case, the amplitude of cylinder oscillation grows with time. Instead, for $-180° < \phi < 0°$, E_c is negative and the energy is transferred to the fluid by the oscillator. As a result the oscillation of cylinder decays with time leading to a steady state. Figure 14(*a*) shows the variation of E_c with U^* for $(Re, m^*) = (60, 20)$. The lock-in regime based on DTI is also shaded in the figure. E_c can be written in terms of the growth rate and frequency of the eigenmode (details in appendix C) as:

$$E_c = 2\pi^2|\hat{Y}|^2 m^* \lambda_r \lambda_i. \tag{6.15}$$

Equation (6.15) shows that the sign of E_c is determined by the sign of λ_r. Therefore, E_c is positive for unstable eigenmode and negative for stable eigenmodes. If an eigenmode is unstable ($\lambda_r > 0$), a net energy transfer takes place from the base flow to the fluid–oscillator system. A part of this energy, determined by the energy ratio E_r, is transferred to the structure. This energy transfer is via the work done by the fluid force in displacing the oscillator. The energy transferred to the oscillator adds up to its kinetic energy as well as the potential energy of the spring. We note that

https://doi.org/10.1017/jfm.2016.157 Published online by Cambridge University Press

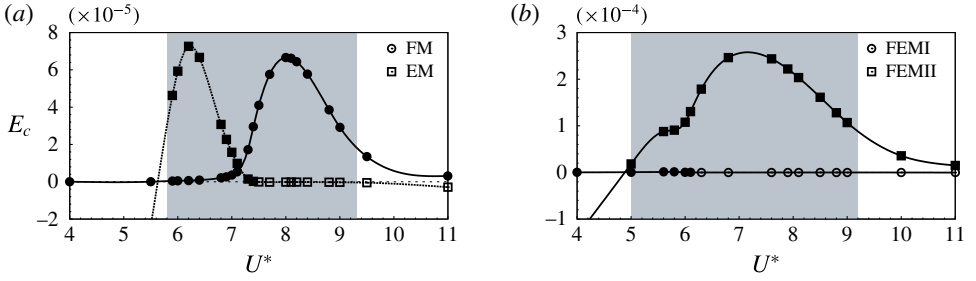

FIGURE 14. Linear stability analysis of the steady flow past a fluid–cylinder system: variation of energy transfer per cycle of cylinder oscillation with U^* for (*a*) $(Re, m^*) = (60, 20)$ and (*b*) $(Re, m^*) = (60, 5)$. The stable and the unstable eigenmodes are shown as hollow and solid symbols, respectively. The lock-in regime from DTI, in the presence of nonlinear effects, is shaded in the figures.

the variation of E_c with U^* can be quite different than the variation of λ_r with U^*, even though they are of the same sign. Therefore, the U^* for largest growth rate may not necessarily coincide with that for maximum energy transfer. It is noted that E_c of the EM is generally higher than that of the fluid mode in the regime of instability of the elastic mode ($5.8 < U^* < 7.3$). However, we recall here that the growth rate of FM is higher than the elastic mode for all U^* (figure 11*c*). This suggests that for $5.8 < U^* < 7.3$ initially FM would dominate the temporal evolution of cylinder displacement. However, as time progresses, EM is expected to drive the structural response towards lock-in. This is confirmed by direct time integration in § 8.3. The variation of E_c with U^* for the case of coupled modes is shown in figure 14(*b*). FEMII is expected to dominate the dynamics of the fluid–structure system in this case.

7. Phase angle between cylinder displacement and lift

In free vibrations, the phase angle between the lift and cylinder displacement is closely related to the energy transfer between the fluid and the oscillator. Morse & Williamson (2009), using the approximation that cylinder motion and fluid forcing are sinusoidal functions, showed that the energy transfer from the fluid to the cylinder over one cycle of cylinder oscillation is given by, $E_{IN} = \pi AF \sin\phi$. Here, A and F are the amplitude of cylinder displacement and lift force, respectively; ϕ denotes the phase difference between the two functions. In the fully developed state, where the system oscillates with constant amplitude and frequency, the energy input to the structural system should exactly balance the energy dissipated by it. Since, in the present study there is no structural damping, E_{IN} is identically zero in the fully developed state. This implies that ϕ can admit only two solutions, 0° or 180°. In general, ϕ is close to zero towards the lower-U^* end of the lock-in regime. However, near the middle of lock-in regime, ϕ suffers a jump of approximately 180°, and remain close to 180° for higher values of U^*. These observations have been reported in earlier articles by Govardhan & Williamson (2000) and Prasanth & Mittal (2008).

Phase angle can be also be defined for eigenmodes obtained from LSA. By substituting (6.7) and (6.8) into the equation describing the motion of the oscillator (2.3) and (2.4), it can be shown that the phase angle related to eigenmodes is given

https://doi.org/10.1017/jfm.2016.157 Published online by Cambridge University Press

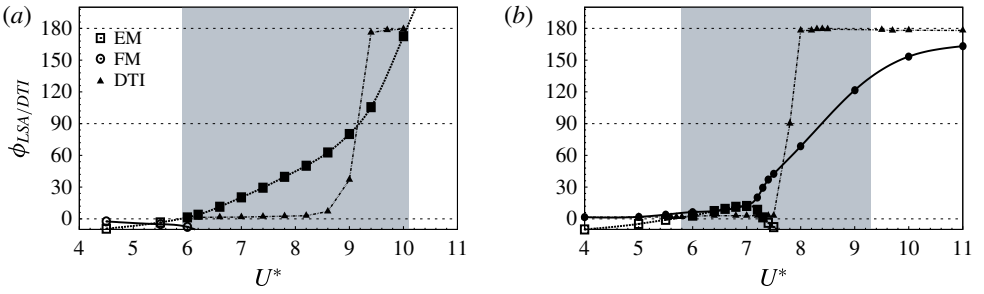

FIGURE 15. Flow past a freely vibrating cylinder: variation of phase angle from DTI and phase angle of eigenmodes with U^* for (*a*) $(Re, m^*) = (40, 10)$ and (*b*) $(Re, m^*) = (60, 20)$. The stable and unstable eigenmodes are denoted by hollow and solid symbols, respectively. The lock-in regime from DTI, in the presence of nonlinear effects, is shaded in the figures.

by:

$$\sin\phi = \frac{2\lambda_i\lambda_r|\hat{Y}|\pi m^*}{|\hat{C}_L|}. \tag{7.1}$$

The details of the derivation are given in appendix C. We denote the phase angle estimated from DTI and that from the eigenmodes as ϕ_{DTI} and ϕ_{LSA}, respectively. As discussed in § 6.2, the eigenmodes are usually associated with non-zero energy transfer. The relationship between E_c and the phase angle is described by (6.14). For unstable eigenmodes the phase angle lies between $0° < \phi_{LSA} < 180°$. Figure 15 shows the variation of phase angle of eigenmodes with U^* for $(Re,\ m^*) = (40,\ 10)$ and $(60,\ 20)$. For comparison ϕ_{DTI} is also plotted. Unlike in DTI, where a phase jump from 0° to 180° occurs during lock-in, ϕ_{LSA} varies rather smoothly with U^*. Figure 15 shows that ϕ_{DTI} undergoes a jump close to that value of U^* where ϕ_{LSA} crosses 90°. It appears that, in most cases, the nonlinear effects drive ϕ_{DTI} to a near-zero value if $\phi_{LSA} < 90°$ and to 180° if $\phi_{LSA} > 90°$ to maintain zero energy transfer in the limit cycle.

Close to the phase jump, the frequency spectrum of the lift force in the fully developed state shows multiple peaks. In general, the phase difference between the lift force and cylinder displacement corresponding to each frequency component is different. The phase angle (ϕ_{DTI}) shown in figure 15 corresponds to the fundamental frequency which is usually the most dominant one. It is observed that for U^* close to the phase jump, ϕ_{DTI} exhibits offset from 0° or 180° despite E_{IN} being equal to zero. We note that the condition of $\phi_{DTI} = 0°$ or 180° for free vibrations has been derived for the situation when the time histories of cylinder displacement and lift force are associated with only one frequency. The offset, therefore, may be attributed to the interaction of components of energy at various frequency.

8. Effect of nonlinearities and relative significance of eigenmodes

8.1. *When do nonlinear terms become significant?*

In the preceding sections we have shown that there are differences between LSA and DTI with respect to the frequency, phase and the extent of lock-in regime. These differences are attributed to the nonlinear terms in DTI of the governing equations.

https://doi.org/10.1017/jfm.2016.157 Published online by Cambridge University Press

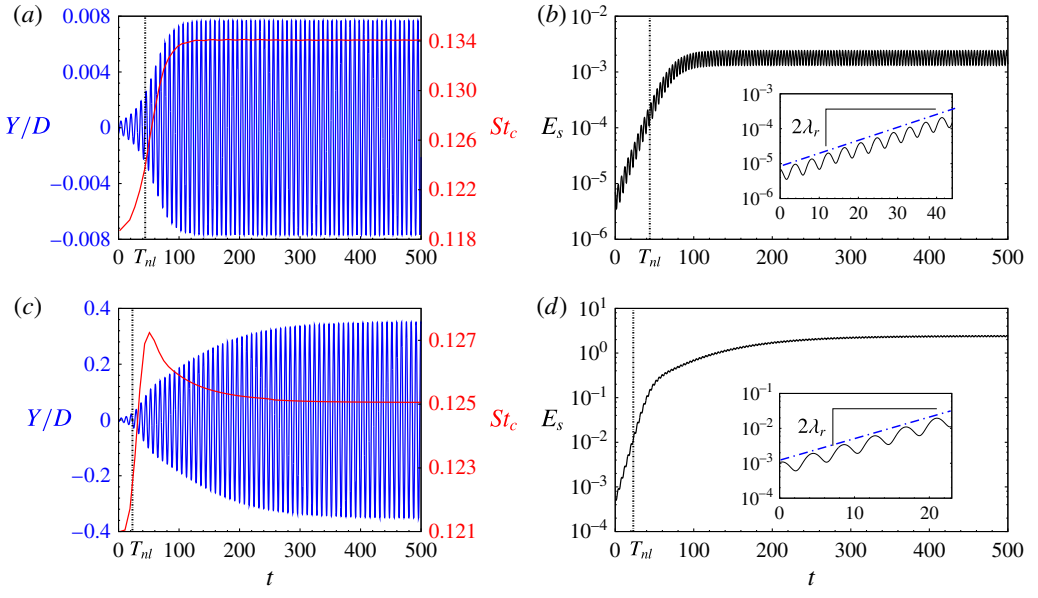

FIGURE 16. (Colour online) $(Re, m^*) = (60, 20)$ flow past a freely vibrating cylinder for (*a*,*b*) $U^* = 5.5$ and (*c*,*d*) $U^* = 8.0$: time evolution of (*a*,*c*) cylinder displacement, Strouhal number based on frequency of cylinder oscillation and (*b*,*d*) structural energy. The time instant beyond which the nonlinear terms become significant is marked in broken lines. Also shown in inset in (*b*,*d*) is the close-up view of the evolution of structural energy in the linear regime. The line with slope two times the growth rate of the wake mode is shown in blue colour.

We recall that the oscillator used in the present study is associated with linear spring and damper. Therefore, the nonlinearity in the fluid–oscillator system results entirely from the convection terms in (2.1). We assume that the nonlinear terms involving the disturbance field become relatively significant when their magnitude exceeds 10 % of the size of the other terms, i.e. $O(|\boldsymbol{u}' \cdot \boldsymbol{\nabla} \boldsymbol{u}'|) \sim 0.1O(|\boldsymbol{U} \cdot \boldsymbol{\nabla} \boldsymbol{U}|)$. Based on this assumption, the time at which the nonlinear effects are expected to become significant is estimated to be:

$$T_{nl} \sim \left(\ln \frac{0.33|U_\infty|}{|\hat{\boldsymbol{u}}_{max}|} \right) \Big/ \lambda_r. \tag{8.1}$$

The details for the derivation of T_{nl} are presented in appendix B. We now present an estimate of T_{nl} for $(Re, m^*) = (60, 20)$ for two values of reduced velocity. Figure 16 shows the estimate of T_{nl} for $U^* = 5.5$ and 8.0. While $U^* = 5.5$ lies before the onset of synchronization, the oscillator experiences lock-in for $U^* = 8.0$ (see figure 11*a*). From figure 16 we observe that up to $t = T_{nl}$ the fluid–structure system indeed retains its linear behaviour. This is most evident from the time variation of the structural energy, E_s. The structural energy at any instant is the sum of the kinetic energy and potential energy of the oscillator. As seen from (6.3), the slope of $\ln(E_s)$ versus t is $2\lambda_r$ in the linear regime. The match between the two slopes, from DTI and the estimate via LSA, is excellent. Beyond $t = T_{nl}$, the nonlinear terms cause saturation in the oscillation amplitude and E_s, leading to a limit cycle. The saturation in the Strouhal number and the added mass coefficient is also observed for $t > T_{nl}$.

https://doi.org/10.1017/jfm.2016.157 Published online by Cambridge University Press

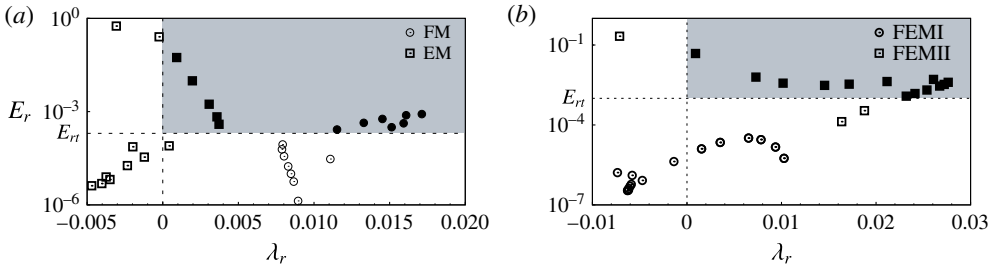

FIGURE 17. Flow past a freely vibrating cylinder: distribution of energy ratio with the growth rate of the eigenmodes for (*a*) $(Re, m^*) = (60, 20)$, and (*b*) $(Re, m^*) = (60, 5)$. All unstable eigenmodes that lead to lock-in with respect to the fully developed state are shown in solid symbols. These eigenmodes are characterized by energy ratio that is greater than a threshold value, E_{rt}.

We note that much of the increase in the amplitude of transverse vibration takes place in the linear regime ($t < T_{nl}$). For example, for $U^* = 5.5$, the amplitude of cylinder response increases eightfold during $0 \leqslant t \leqslant T_{nl}$ and only by a factor of 1.5 beyond T_{nl} up to the attainment of limit cycle. These numbers for $U^* = 8.0$ are 17 and 3, approximately.

8.2. *What causes lock-in?*

The observations from the preceding section motivate us to propose a hypothesis to as to why lock-in occurs for a certain range of U^*, and not for others. We believe that E_r (fraction of energy in the structural part of the eigenmode) determines if a certain disturbance field will lead to attainment of lock-in. To demonstrate the relevance of the energy ratio, E_r, we consider the case of $(Re, m^*) = (60, 20)$. The two modes that, in general, govern the aeroelastic instability of the fluid–structure system for various U^* are EM and FM. Figure 17(*a*) shows the points for the two eigenmodes on the E_r–λ_r plane, for various U^*. DTI is carried out for each case. The initial condition is the steady flow superimposed with the eigenmode:

$$(\boldsymbol{u}(\boldsymbol{x}), p(\boldsymbol{x}), \dot{Y}, Y)^{\mathrm{T}} = (\boldsymbol{U}(\boldsymbol{x}), P(\boldsymbol{x}), 0, 0)^{\mathrm{T}} + s * (\hat{\boldsymbol{u}}(\boldsymbol{x}), \hat{p}(\boldsymbol{x}), \hat{\dot{Y}}, \hat{Y})^{\mathrm{T}}. \tag{8.2}$$

s is a scalar and is used to control the magnitude of the initial disturbance. Unless stated otherwise, a value of 1.0 is assigned to s for all the cases presented in this work. In figure 17(*a*) the eigenmodes that lead to lock-in are marked in solid symbols and the ones that do not cause lock-in are marked in hollow symbol. It is noted that all unstable eigenmodes, irrespective of their growth rate, that have an E_r beyond a threshold value of 2×10^{-4} lead to lock-in. Interestingly, the case that leads to maximum oscillation amplitude is associated with smallest positive value of λ_r, but the largest value of E_r. Similarly, modes that are associated with relatively large λ_r, but with E_r below the threshold value, do not lead to lock-in. The region in the E_r–λ_r plane that leads to lock-in is marked in figure 17(*a*). Figure 17(*b*) shows the same for $(Re, m^*) = (60, 5)$. Similar observations hold for this figure as well. The value of E_{rt} in this case is 1×10^{-3}. We note that the threshold value of E_r, required for lock-in depends on m^*, and possibly on Re.

https://doi.org/10.1017/jfm.2016.157 Published online by Cambridge University Press

8.3. *Eigenmodes responsible for lock-in*

For subcritical Re ($Re \leqslant Re_o$), the instability of the fluid–structure system, if any, is caused by only one unstable eigenmode. In the scenario of coupled modes, FEMII is responsible for lock-in. For large mass ratios, where the modes are decoupled, lock-in is attributed to the growth of EM. For supercritical Re ($Re > Re_o$), the situation becomes complicated as LSA predicts lock-in for all U^*. Further, in certain flow regimes multiple eigenmodes are unstable. We now study in more detail the mechanism of how an unstable eigenmode leads to lock-in for $Re > Re_o$. We carry out DTI for $(Re, m^*) = (60, 20)$ for various values of U^* in the lock-in regime. As shown in figure 11(*c*), for $(Re, m^*) = (60, 20)$, LSA predicts the instability of the FM for the fluid–structure system for all values of U^*. The EM is unstable for $5.8 < U^* < 7.3$. The growth rate of FM is higher than that of EM in the entire U^* regime. However, the energy ratio, E_r, that has been shown to be very relevant for determining the amplitude of cylinder oscillation in the limit cycle, is larger for EM than for FM, and above the threshold value for $5.8 < U^* < 7.2$. This is shown in figure 13(*a*). Figure 17(*a*) shows that lock-in occurs only when E_r for the concerned mode exceeds the threshold value. The range for lock-in for $(Re, m^*) = (60, 20)$ is $5.8 < U^* < 9.3$.

8.3.1. *Lock-in via fluid mode*

For $(Re, m^*) = (60, 20)$, lock-in via the fluid mode occurs for $7.3 \leqslant U^* < 9.3$. In this regime, the energy ratio of FM is larger than the threshold value while the elastic mode is stable. Figure 16 shows the time evolution of the cylinder response, Strouhal number and energy of the structure for DTI initiated with the steady flow superimposed with FM for $U^* = 5.5$ and 8.0. In both cases, the time variation of E_s, in the linear regime, is consistent with the response predicted by LSA. Lock-in is observed at $U^* = 8.0$ and is accompanied with large amplitude vibration of the cylinder. No lock-in is obtained for $U^* = 5.5$.

8.3.2. *Lock-in via elastic mode*

For $(Re, m^*) = (60, 20)$, both the elastic and the fluid mode are unstable for $5.8 < U^* < 7.3$. In this regime E_r of the elastic mode is above the threshold energy for lock-in (figure 17*a*). The fluid mode, though unstable, has energy ratio lower than E_{rt}. Hence, lock-in over this regime results from the instability of EM. To elucidate this, we carry out computations for $U^* = 6.0$ with two initial conditions. In the first case, the simulation is initiated with the elastic mode superimposed on the steady solution. The value of s (8.2) used for this case is 10.0. Figure 18 shows the time evolution of Y/D and E_s. It is observed that the amplitude of cylinder oscillation increases with time up to $t = T_{nl}$ with a rate that matches the growth rate of EM. Concomitantly, the structural energy grows with twice the growth rate of EM over this time interval. Beyond $t = T_{nl}$, the response of the fluid–structure system approaches a limit cycle where the cylinder exhibits relatively large amplitude of oscillation with frequency that is close to the natural frequency of the oscillator in vacuum. The fluid–structure system is in a state of lock-in in the limit cycle. Simulations with lower value of s (for example, $s = 1$) lead to an interesting evolution. The numerical inaccuracies in the eigenmodes act as noise and excite other modes, including FM. Since FM has a higher growth rate than EM, for this case, the FM grows very rapidly compared to EM. Therefore, in the linear regime for $s = 1.0$, the growth of amplitude of the cylinder exhibits the growth rate of EM at low t followed by a growth rate corresponding to that of FM up to the end of the linear regime. On the other hand, with $s = 10.0$, even

https://doi.org/10.1017/jfm.2016.157 Published online by Cambridge University Press

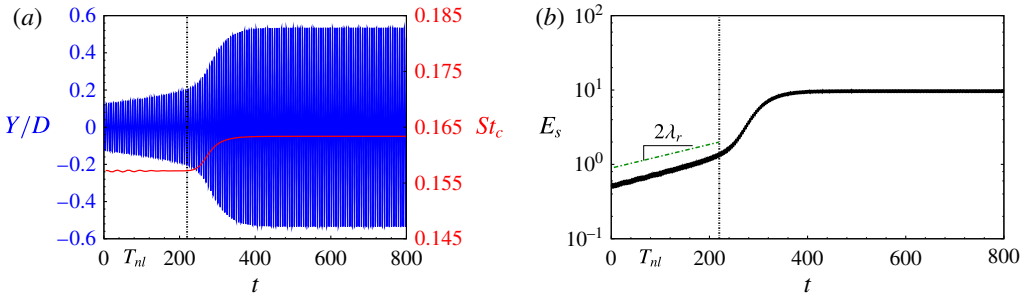

FIGURE 18. (Colour online) Flow past a freely vibrating cylinder for $(Re, m^*, U^*) = (60, 20, 6.0)$ initiated with EM: time evolution of (*a*) cylinder displacement, Strouhal number based on frequency of cylinder oscillation and (*b*) structural energy. The time instant beyond which the nonlinear terms become significant is marked in dash-dotted lines. The line with slope two times the growth rate of the elastic mode is shown in green colour.

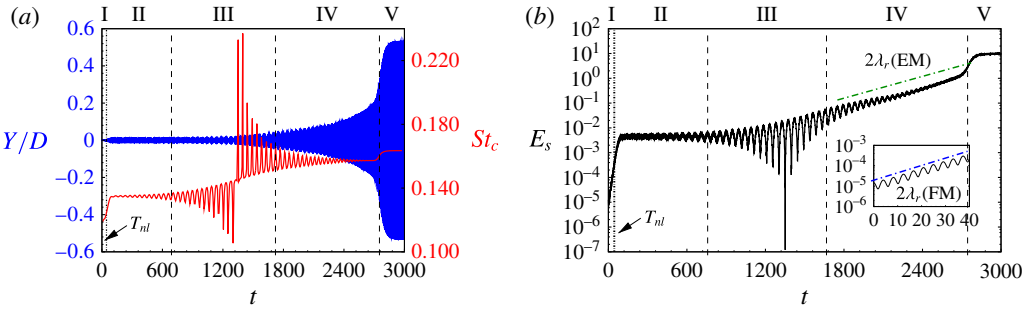

FIGURE 19. (Colour online) Flow past a freely vibrating cylinder for $(Re, m^*, U^*) = (60, 20, 6.0)$ initiated with FM: time evolution of (*a*) cylinder displacement, Strouhal number based on frequency of cylinder oscillation and (*b*) structural energy. The time instant beyond which the nonlinear terms become significant is marked in dash-dotted lines. The different flow regions are demarcated by broken lines. The line with slope two times the growth rate of the elastic mode is shown in green colour. Also shown in inset is the evolution of structural energy in the linear regime. The line with slope two times the growth rate of the fluid mode is shown in blue colour.

though the FM grows faster than the EM, the growth is dominated by EM owing to its significantly larger initial strength.

In the second case, the computations are initiated with the fluid mode superimposed on the steady solution. Figure 19 shows the time history of Y/D and E_s for this case. It is observed that the initial growth of the amplitude of cylinder oscillation is governed by the fluid mode. This is shown as region I in the figure (also shown in the inset). In this region, the contribution of nonlinear terms based on the analysis, described earlier, is negligible. In region II, the oscillations achieve a state where the amplitude and the structural energy are nearly constant. It is further observed that Y/D and E_s in region II are comparable to that observed for $U^* = 5.5$ in the fully developed state; the latter corresponds to a lock-in state. Beyond region II, the response of the cylinder exhibit beats. The frequency spectrum of Y/D show two prominent peaks: one at 0.136 and the other at 0.157. The former is equal to the frequency of oscillation

https://doi.org/10.1017/jfm.2016.157 Published online by Cambridge University Press

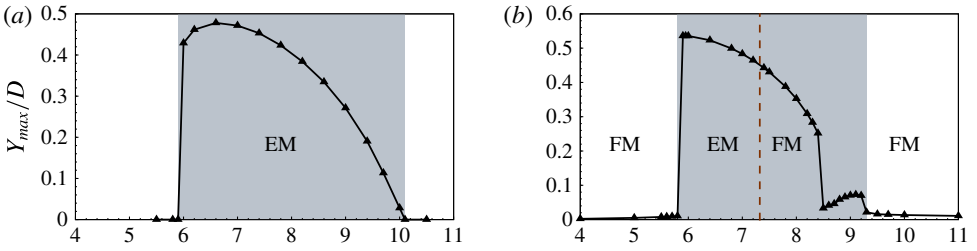

FIGURE 20. (Colour online) Flow past a freely vibrating cylinder: different response regimes and the eigenmodes responsible for them for (*a*) $(Re,\ m^*) = (40,\ 10)$ and (*b*) $(Re, m^*) = (60, 20)$. The lock-in regime from DTI, in the presence of nonlinear effects, is shaded in the figure.

in region II, while the latter matches the frequency of the elastic mode for $U^* = 6.0$. It is noted that the structural energy, in region III, grows almost linearly with twice the growth rate of the elastic mode. The linear growth becomes more clear in region IV. Further the frequency spectrum in region IV is dominated by the elastic mode. These observations suggest that the dynamics of the fluid–structure system in regions III and IV is governed by the elastic mode. The transition of the system from region II to region IV may be attributed to transfer of the energy from FM to EM due to nonlinear effects which become significant beyond T_{nl}. We recall that the energy transfer per cycle of cylinder oscillation (E_c) for EM is quite large (figure 14). As a result, the structural energy of the system increases significantly in region IV. At the end of region IV the oscillation amplitude and structural energy are similar to the values observed at the end of the linear regime for computations started with the elastic mode. Finally, in region *V*, the oscillations achieve a limit cycle with amplitude $Y/D \sim 0.5$. In summary, the computations initiated with the FM drive the system to an intermediate state corresponding to no lock-in. The system then transitions to a state of lock-in via the elastic mode.

9. Conclusions

The phenomenon of synchronization/lock-in in transverse-only free vibrations of a circular cylinder is investigated in the laminar flow regime. DTI and LSA, of the equations governing the dynamics of the coupled aeroelastic system, is carried out. Lock-in is identified from the results of DTI using the metrics that have been proposed and utilized in earlier studies. It is characterized by relatively high amplitude of cylinder response and the matching of the frequencies of the periodic wake vortex mode and cylinder oscillation (Khalak & Williamson 1999) when it has achieved a limit cycle. Figure 20 shows an example each of the lock-in regime for the sub and supercritical *Re*.

A stabilized finite element method for carrying out LSA of an aeroelastic system has been presented. The linear instability of the aeroelastic system implies that in the absence of nonlinear effects, the system achieves very large amplitude oscillations. The nonlinear terms in the equations governing the flow of fluid, become significant when the disturbance field grows beyond a certain limit. They tend to saturate the growth of the disturbance field and drive the system to a limit cycle. The oscillation amplitude of the cylinder, in the limit cycle, is quite large over a certain range of U^*. During synchronization, the frequency of the system evolves from F_{LSA} to close to F_N.

https://doi.org/10.1017/jfm.2016.157 Published online by Cambridge University Press

Outside the lock-in regime, however, the frequency evolves to a value that is close to the vortex shedding frequency for the flow past a stationary cylinder. The reason as to why this happens is not clear from this study. We speculate that this might be an outcome of the fluid–structure system attempting to find a state where the fluid faces least resistance from the structure and achieves this by minimization of the added mass during the limit cycle in free vibrations.

A method, based on the order-of-magnitude analysis of the governing equations, to estimate the time beyond which nonlinear terms become significant has been presented. It is observed, via computations initiated with an unstable eigenmode, that the increase in the amplitude of cylinder oscillation occurs mainly in the linear regime. Further, not all unstable eigenmodes lead to lock-in in the limit cycle. We define energy ratio as the fraction of the total energy of the eigenmode that is contained in the structure as kinetic and potential energy. Only those unstable eigenmodes for which the energy ratio is above a certain threshold value result in lock-in in the saturated state. This behaviour is found to be independent of the value of the growth rate of the unstable eigenmode. For subcritical Re, the regime of U^* for which lock-in occurs, coincides with the region of linear instability of the fluid–structure system. In this case, only one mode is linearly unstable and that too for a finite range of U^*. For supercritical Re, the aeroelastic system in unstable for all U^*. However, lock-in occurs over a finite range of U^*. Lock-in, in this case, is caused by different eigenmodes for different regimes of U^*. This is shown in figure 20. In the flow regime where multiple modes are unstable, the energy transfer from the fluid to the structure corresponding to the eigenmode is found to have significant effect on the time evolution of the response.

Compared to the stationary cylinder, the transversely oscillating cylinder is associated with two additional eigenmodes. A new approach to classification of modes is presented wherein Re and m^* are fixed and LSA is carried out over a wide range of U^*. The present classification makes it relatively easier to compare the characteristics of fluid–structure system in the lock-in regime. It is observed that for certain combinations of Re and m^*, the eigenmodes corresponding to the two leading eigenvalues are distinct and maintain the distinction for all U^*. The two modes, in this situation, are referred to as the fluid mode, FM and the elastic mode, EM. The frequency of the fluid mode remains close to that of the stationary wake mode for all reduced velocities. The frequency of the elastic mode, on the other hand, varies inversely with U^*. However, for certain combinations of Re and m^*, it may not be possible to classify the two modes as either FM or EM. In this situation we refer to the two modes as coupled modes. The evolution of modes is better understood on λ_r–U^*_{LSA} plane. On this plane, in the case of decoupled modes, the fluid mode appears like a ring, separate from the elastic mode. In the case of coupled modes, the two modes appear to be parts of a single curve. In general, coupled modes are observed for low m^* and decoupled modes for relatively large m^*. We define critical mass ratio, m^*_c, as the largest mass ratio for which the modes are coupled. m^*_c is found to be very large for Re_o, the critical Re for the onset of vortex shedding past a stationary cylinder. It decreases as Re deviates further from Re_o.

The phase angle related to the eigenmodes has been defined. The phase angle of the eigenmode is found to be related to the energy transfer per oscillation cycle of the cylinder oscillation. Unlike in the nonlinear regime where a jump in phase with U^* is observed, the Φ for the eigenmodes for LSA varies smoothly with U^*. It is observed in most cases that in the limit cycle the nonlinear processes drive the phase angle to near zero value if the phase angle is less than 90°, and to 180° if the phase angle is greater than 90°. The phenomenon of phase jump in the limit cycle response is observed when the phase angle of an unstable eigenmode crosses 90°.

https://doi.org/10.1017/jfm.2016.157 Published online by Cambridge University Press

Mode	M1		M2	
	λ_r	F_{LSA}	λ_r	F_{LSA}
FM	0.0412	0.1213	0.0410	0.1213
EM	0.0134	0.1331	0.0132	0.1331

TABLE 1. $(Re, m^*, U^*) = (60, 20, 7.0)$ LSA of a fluid–structure system: effect of mesh resolution on the rightmost eigenvalue of different modes. Meshes M1 and M2 consist of 12 814 and 15 004 nodes, respectively.

Acknowledgements

The use of computational resources at High Performance Computing facility, Computer Center, Indian Institute of Technology Kanpur that is set up with assistance from DST, India is acknowledged. The authors are also grateful to Dr D. Philip, Department of Industrial and Management Engineering for providing access to his computational resources.

Appendix A. Convergence studies

The computations in this study have been carried out over a wide range of parameter space ($20 \leqslant Re \leqslant 100$, $1.0 \leqslant m^* \leqslant 300$, $2.0 \leqslant U^* \leqslant 15.0$). Prasanth & Mittal (2008) carried out a detailed domain and mesh convergence study for numerical simulations at $60 \leqslant Re \leqslant 100$. They reported that a computational domain with blockage less than 2 % can successfully simulate an unbounded flow. In the present study, we have used a computational domain that has a blockage of 1 %. The spatial resolution of the mesh used for carrying out direct time integration is higher than the one used by Prasanth & Mittal (2008). It consists of 12 814 nodes and 12 540 elements. The same mesh is used for carrying out linear stability analysis. We name this mesh M1. To establish the adequacy of mesh M1 for LSA, its performance is compared to a mesh with higher spatial resolution. The finer mesh is denoted by M2. The number of nodes and elements in mesh M2 are 15 004 and 14 710, respectively. The computational domain as well as the structure of the mesh is same in the two cases. The difference is mostly in the grid points close to the cylinder. Table 1 shows the effect of spatial resolution on the growth rate and frequency of the eigenmodes computed at $U^* = 7.0$ for $(Re, m^*) = (60, 20)$. The value of U^* is close to the one for which maximum growth rate is obtained for EM. Results from the two meshes are in very good agreement. The maximum difference of 0.5 % is noted in the growth rate of EM. In view of the difference being small enough, mesh M1 is employed for all computations in the present work.

Appendix B. Derivation of T_{nl}

We present a method to obtain an *a priori* estimate of the time beyond which the nonlinear terms are expected to become significant. Let $\boldsymbol{U}$ represent the base flow velocity and L denote a suitable length scale. Then the convection term in the base flow is of the order $|\boldsymbol{U} \cdot \boldsymbol{\nabla U}| \sim O({U_\infty}^2/L)$; where U_∞ is the free-stream speed. For the flow regime considered in the present work, this is also the magnitude of the largest term in the flow equations. We assume that the nonlinear terms involving the disturbance field become relatively significant when their magnitude exceeds 10 % size of the other terms, i.e. $O(|\boldsymbol{u}' \cdot \boldsymbol{\nabla u}'|) \sim 0.1O(|\boldsymbol{U} \cdot \boldsymbol{\nabla U}|)$. This implies that the nonlinear

https://doi.org/10.1017/jfm.2016.157 Published online by Cambridge University Press

terms gain significance when $O(|\boldsymbol{u}'|) \sim 0.33U_\infty$. We consider the situation when the computations are initiated with the steady base flow superimposed with a disturbance field corresponding to the eigenmode from LSA. Therefore, in the linear regime the disturbance evolves as $\boldsymbol{u}' = \hat{\boldsymbol{u}}e^{\lambda t}$. The estimate of the size of the disturbance at any time is given as: $O(|\boldsymbol{u}'|) \sim O(|\hat{\boldsymbol{u}}|)e^{\lambda_r t}$. The nonlinear terms are expected to become locally important as soon as $\hat{\boldsymbol{u}}$ becomes large enough at that local location. This will occur at the spatial location where $|\hat{\boldsymbol{u}}|$ is the largest. We, therefore, locate the maxima of $|\hat{\boldsymbol{u}}|$, and represent it as $|\hat{\boldsymbol{u}}_{max}|$. Let T_{nl} be the time at which the nonlinear terms gain significance. At that time instant, $O(|\boldsymbol{u}'|) \sim |\hat{\boldsymbol{u}}_{max}|e^{\lambda_r T_{nl}}$ and the disturbance becomes large locally as $\sim 0.33U_\infty$. Therefore, the estimate of T_{nl} is

$$T_{nl} \sim \left(\ln \frac{0.33|U_\infty|}{|\hat{\boldsymbol{u}}_{max}|}\right) \Big/ \lambda_r. \tag{B 1}$$

Appendix C. Amplitude and frequency equations

The time evolution of cylinder displacement and lift coefficient corresponding to an eigenmode $(\hat{\boldsymbol{u}}, \hat{p}, \hat{Y}, \hat{Y})$ is given as:

$$Y(t) = \frac{(\hat{Y}e^{\lambda t} + \text{c.c.})}{2}, \tag{C 1}$$

$$C_L(t) = \frac{(\hat{C}_L e^{\lambda t} + \text{c.c.})}{2}. \tag{C 2}$$

Here, $\hat{C}_L$ is the lift coefficient calculated by integrating the stress corresponding to the eigenmode around the boundary of the cylinder. In general, $\hat{Y}$ and $\hat{C}_L$ are complex and c.c. represents the complex conjugate. Let $|\hat{Y}|$ and $|\hat{C}_L|$ represent the magnitude of $\hat{Y}$ and $\hat{C}_L$, respectively. Further, let θ and $\theta + \phi$ denote the argument of $\hat{Y}$ and $\hat{C}_L$, respectively, where ϕ is the phase angle between the cylinder displacement and lift coefficient. We recall that $\lambda = \lambda_r + \mathrm{i}\lambda_i$. Equations (C 1) and (C 2) can be rewritten as

$$Y(t) = |\hat{Y}|e^{\lambda_r t}\cos(\lambda_i t + \theta), \tag{C 3}$$

$$C_L(t) = |\hat{C}_L|e^{\lambda_r t}\cos(\lambda_i t + \theta + \phi). \tag{C 4}$$

Substituting (C 3) and (C 4) in the equations describing the motion of the cylinder (2.3) and (2.4), and assuming the structural damping coefficient to be zero, we obtain:

$$\begin{aligned} &|\hat{Y}|e^{\lambda_r t}[(\lambda_r{}^2 - \lambda_i{}^2)\cos(\lambda_i t + \theta) - 2\lambda_r\lambda_i \sin(\lambda_i t + \theta)] + (2\pi F_N)^2|\hat{Y}|e^{\lambda_r t}\cos(\lambda_i t + \theta) \\ &= \frac{|\hat{C}_L|e^{\lambda_r t}}{\pi m^*}[\cos(\lambda_i t + \theta)\cos\phi - \sin(\lambda_i t + \theta)\sin\phi]. \end{aligned} \tag{C 5}$$

Since (C 5) holds for all time, we collect the terms involving $\cos(\lambda_i t + \theta)$ and $\sin(\lambda_i t + \theta)$ and equate them to zero. This leads to

$$\sin\phi = \frac{2\lambda_i\lambda_r|\hat{Y}|\pi m^*}{|\hat{C}_L|}, \tag{C 6}$$

$$\lambda_i{}^2 = (2\pi F_N)^2\alpha, \tag{C 7}$$

https://doi.org/10.1017/jfm.2016.157 Published online by Cambridge University Press

where, $\alpha = [(\lambda_r{}^2 - (|\hat{C}_L|\cos\phi)/(|\hat{Y}|\pi m^*))/(2\pi F_N{}^2)] - 1$. We refer (C 6) and (C 7) as the amplitude and frequency equation following the nomenclature proposed by Khalak & Williamson (1999). While (C 6) defines the phase between the cylinder displacement and the lift acting on it, (C 7) relates the frequency of the response of the fluid–structure system to its natural frequency in the vacuum.

Using (C 6), the energy transfer per cycle of cylinder oscillation for an eigenmode, E_c, that is given by (6.14), can also be written as

$$E_c = 2\pi^2|\hat{Y}|^2 m^* \lambda_r \lambda_i. \tag{C 8}$$

REFERENCES

BEARMAN, P. W. 1984 Vortex shedding from oscillating bluff bodies. *Annu. Rev. Fluid Mech.* **16** (1), 195–222.

BEARMAN, P. W. 2011 Circular cylinder wakes and vortex-induced vibrations. *J. Fluids Struct.* **27** (5), 648–658.

BISHOP, R. E. D. & HASSAN, A. Y. 1964 The lift and drag forces on a circular cylinder oscillating in a flowing fluid. *Proc. R. Soc. Lond.* A **277**, 51–75.

COSSU, C. & MORINO, L. 2000 On the instability of a spring-mounted circular cylinder in a viscous flow at low Reynolds numbers. *J. Fluids Struct.* **14** (2), 183–196.

ÉTIENNE, S. & PELLETIER, D. 2012 The low Reynolds number limit of vortex-induced vibrations. *J. Fluids Struct.* **31**, 18–29.

FENG, C. C. 1968 The measurement of vortex induced effects in flow past stationary and oscillating circular and D-section cylinders. Master's thesis, University of British Columbia, Vancouver, BC, Canada.

GOVARDHAN, R. & WILLIAMSON, C. H. K 2000 Modes of vortex formation and frequency response of a freely vibrating cylinder. *J. Fluid Mech.* **420**, 85–130.

GOVARDHAN, R. & WILLIAMSON, C. H. K. 2002 Resonance forever: existence of a critical mass and an infinite regime of resonance in vortex-induced vibration. *J. Fluid Mech.* **473**, 147–166.

KHALAK, A. & WILLIAMSON, C. H. K. 1997 Fluid forces and dynamics of a hydroelastic structure with very low mass and damping. *J. Fluids Struct.* **11** (8), 973–982.

KHALAK, A. & WILLIAMSON, C. H. K. 1999 Motions, forces and mode transitions in vortex-induced vibrations at low mass-damping. *J. Fluids Struct.* **13** (7), 813–851.

KUMAR, B. & MITTAL, S. 2006 Prediction of the critical Reynolds number for flow past a circular cylinder. *Comput. Meth. Appl. Mech. Engng* **195** (44), 6046–6058.

LU, L. & PAPADAKIS, G. 2014 An iterative method for the computation of the response of linearised Navier–Stokes equations to harmonic forcing and application to forced cylinder wakes. *Intl J. Numer. Meth. Fluids* **74** (11), 794–817.

MARAIS, C., GODOY-DIANA, R., BARKLEY, D. & WESFREID, J. E. 2011 Convective instability in inhomogeneous media: impulse response in the subcritical cylinder wake. *Phys. Fluids* **23** (1), 014104.

MELIGA, P. & CHOMAZ, J. 2011 An asymptotic expansion for the vortex-induced vibrations of a circular cylinder. *J. Fluid Mech.* **671**, 137–167.

MITTAL, S. & KUMAR, B. 2007 Astabilized finite element method for global analysis of convective instabilities in nonparallel flows. *Phys. Fluids* **19** (8), 088105.

MITTAL, S. & TEZDUYAR, T. E 1992*a* Afinite element study of incompressible flows past oscillating cylinders and aerofoils. *Intl J. Numer. Meth. Fluids* **15** (9), 1073–1118.

MITTAL, S. & TEZDUYAR, T. E 1992*b* Notes on the stabilized space–time finite-element formulation of unsteady incompressible flows. *Comput. Phys. Commun.* **73** (1–3), 93–112.

MITTAL, S. & VERMA, A. 2014 Afinite element formulation for global linear stability analysis of a nominally two-dimensional base flow. *Intl J. Numer. Meth. Fluids* **75** (4), 295–312.

https://doi.org/10.1017/jfm.2016.157 Published online by Cambridge University Press

MORSE, T. L. & WILLIAMSON, C. H. K. 2009 Prediction of vortex-induced vibration response by employing controlled motion. *J. Fluid Mech.* **634**, 5–39.

NAVROSE, YOGESWARAN, V., SEN, S. & MITTAL, S. 2014 Free vibrations of an elliptic cylinder at low Reynolds numbers. *J. Fluids Struct.* **51**, 55–67.

PRASANTH, T. K. & MITTAL, S. 2008 Vortex-induced vibrations of a circular cylinder at low Reynolds numbers. *J. Fluid Mech.* **594**, 463–491.

PRASANTH, T. K., PREMCHANDRAN, V. & MITTAL, S. 2011 Hysteresis in vortex-induced vibrations: critical blockage and effect of m^*. *J. Fluid Mech.* **671**, 207–225.

SARPKAYA, T. 1995 Hydrodynamic damping, flow-induced oscillations, and biharmonic response. *J. Offshore Mech. Arctic Engng* **117** (4), 232–238.

SARPKAYA, T. 2004 Acritical review of the intrinsic nature of vortex-induced vibrations. *J. Fluids Struct.* **19** (4), 389–447.

SINGH, S. P. & MITTAL, S. 2005 Vortex-induced oscillations at low Reynolds numbers: hysteresis and vortex-shedding modes. *J. Fluids Struct.* **20** (8), 1085–1104.

TEZDUYAR, T. E., BEHR, M., MITTAL, S. & LIOU, J. 1992*a* Anew strategy for finite element computations involving moving boundaries and interfaces – the deforming-spatial-domain/space–time procedure: II. Computation of free-surface flows, two-liquid flows, and flows with drifting cylinders. *Comput. Meth. Appl. Mech. Engng* **94** (3), 353–371.

TEZDUYAR, T. E., LIOU, J. & BEHR, M. 1992*b* Anew strategy for finite element computations involving moving boundaries and interfaces–the dsd/st procedure: I. The concept and the preliminary numerical tests. *Comput. Meth. Appl. Mech. Engng* **94** (3), 339–351.

TEZDUYAR, T. E., MITTAL, S., RAY, S. E. & SHIH, R. 1992*c* Incompressible flow computations with stabilized bilinear and linear equal-order-interpolation velocity-pressure elements. *Comput. Meth. Appl. Mech. Engng* **95** (2), 221–242.

WILLIAMSON, C. H. K. & GOVARDHAN, R. 2004 Vortex-induced vibrations. *Annu. Rev. Fluid Mech.* **36**, 413–455.

WILLIAMSON, C. H. K. & ROSHKO, A. 1988 Vortex formation in the wake of an oscillating cylinder. *J. Fluids Struct.* **2** (4), 355–381.

WU, X., GE, F. & HONG, Y. 2012 Areview of recent studies on vortex-induced vibrations of long slender cylinders. *J. Fluids Struct.* **28**, 292–308.

ZHANG, W., LI, X., YE, Z. & JIANG, Y. 2015 Mechanism of frequency lock-in in vortex-induced vibrations at low Reynolds numbers. *J. Fluid Mech.* **783**, 72–102.

https://doi.org/10.1017/jfm.2016.157 Published online by Cambridge University Press